Strain within the Ultrahigh-Pressure Western Gneiss Region of Norway recorded by Quartz CPOs

Nicolas C. Barth[1], Bradley R. Hacker[1], Gareth G.E. Seward[1], Emily O. Walsh[2], David Young[3] & Scott Johnston[4]

[1] *Department of Earth Science, University of California, Santa Barbara CA 93106, USA*

(e-mail: hacker@geol.ucsb.edu)

[2] *Department of Geology, Cornell College, Mount Vernon, IA, 52314, USA*

[3] *Department of Geology, University of Texas, San Antonio, TX, 78249, USA*

[4] *Department of Physics, California Polytechnic State University, San Luis Obispo, CA, 93407, USA*

Abstract: Electron back-scatter diffraction was used to measure the crystal preferred orientations (CPOs) from 101 samples across the ultrahigh-pressure Western Gneiss Region of Norway to assess slip systems, sense of shear, CPO strength, and strain geometry. The CPOs suggest a dominance of prism <a> slip, with lesser amounts of prism [c] slip and basal <a> slip; there are few Type-I and Type-II girdles. The major structural feature in the study area—the high-strain, top-W, normal-sense Nordfjord–Sogn Detachment Zone—is characterized by asymmetric and strong CPOs; an eastern domain with strong asymmetric CPOs shows top-E shear. Strain throughout the study area was characterized by a mix of plane strain and constriction with no evidence of flattening. Adjacent gneiss and quartzite/vein samples have similar CPOs.

Dislocation creep can produce crystal preferred orientations (CPOs) because the difference between vorticity imposed on a crystal by deformation and the vorticity produced by dislocation glide is balanced by rotation of the crystal lattice (*Taylor* 1938; *Lister* 1982). The CPO that results is a function of factors such as the active deformation mechanisms (including dislocation slip systems), strain magnitude, rate of recrystallization, and strain geometry. As such, the CPOs of minerals—in particular, quartz, calcite, and olivine—can be used to deconvolve some of these factors and reconstruct the deformation of naturally deformed rocks.

Much emphasis has been placed on understanding and interpreting quartz CPOs because of the abundance of quartz in the continental crust. The most-important slip systems in quartz are basal (0001) <a> slip, prism $\{10\bar{1}0\}$ <a> slip, positive rhomb $\{10\bar{1}1\}$ <a> slip, negative rhomb $\{01\bar{1}1\}$ <a> slip, prism $\{10\bar{1}0\}$ [c] slip, and Dauphiné twinning (Christie et al. 1964; Baëta & Ashbee 1969; Blacic & Christie 1984; Linker et al. 1984; Lloyd 2004). Activation of these slip systems is temperature dependent such that basal <a> glide at low temperatures gives way to prism <a> slip with increasing temperature, and eventually, to dominant prism [c] slip (*Blacic* 1975; *Blumenfeld et al.* 1986). Assuming that the slip plane rotates toward the shear plane and that the slip direction rotates toward the shear direction of an imposed deformation, the activity of that slip system can be inferred from a CPO. This assumption is unjustified in general, however, because crystals are constrained by neighboring grains and multiple slip systems are typically active simultaneously (Lister et al. 1978; Lister & Hobbs 1980; Wenk et al. 1989; Wenk & Christie 1991; Casey & McGrew 1999). Instead, CPOs reflect variations in the rates of lattice rotation, with slow rates of rotation forming maxima (Wenk & Christie 1991).

Progressive strain of a polycrystal leads to progressive rotation of the crystal lattices and, therefore, to a relationship between strain magnitude and CPO strength

(Lister et al. 1978); this relationship has been demonstrated in experimentally and naturally deformed rocks (Marjoribanks 1976; Bouchez 1977; Carreras et al. 1977; Miller & Christie 1981; Law 1986; Dell'Angelo & Tullis 1989; Heilbronner & Tullis 2006). Other factors that influence CPO strength include the particular slip systems that are active, the activity of other deformation mechanisms, the rate of recrystallization, the presence of other phases, and variations in strain path (e.g., Knipe & Law 1987; Casey & McGrew 1999). Also, CPO strength is expected to reach a steady state, beyond which further strain will not be recorded (Wenk & Christie 1991).

Quartz CPOs in experimentally deformed rocks (*Tullis et al.* 1973), naturally deformed rocks (Bouchez et al. 1983), and simulated rocks (Lister et al. 1978; Wenk et al. 1989) can reflect whether the imposed strain was coaxial or noncoaxial. This relationship has been exploited to infer the sense of shear in naturally deformed rocks, by using the sense of asymmetry between the flow plane inferred from the CPO skeleton and the flattening plane defined by the foliation (Behrmann & Platt 1982). This techniques is expected to be inaccurate to some degree because the relationship between the CPO skeleton and the kinematic framework is likely to be more complex than assumed (Wenk & Christie 1991).

Quartz CPOs in experimentally (Dell'Angelo & Tullis 1989; Heilbronner & Tullis 2006) and naturally (Price 1985; Law 1986) deformed rocks have been shown to depend on strain geometry or distortion; simulations have also shown a dependence of CPOs on strain geometry (Lister et al. 1978; Bascou et al. 2002). In favorable circumstances the reverse relationship—using quartz CPOs to determine strain geometry or distortion—can be exploited (Schmid & Casey 1986). If one makes the simplifying assumption that principal slip planes rotate until they are parallel to the shear plane and slip directions rotate parallel to the shear direction, a CPO that results from plane strain should have the form of a single crystal if only one slip

system is active (Fig. 1). During pure flattening, slip planes rotate away from the shortening direction, and the absence of a unique extension direction means that the slip directions are dispersed evenly; thus, the slip directions define a girdle if only one slip system is active (Fig. 1). Conversely, during pure constriction, the slip directions become aligned, and the absence of a unique flattening plane means that the slip planes are dispersed evenly; thus, the poles to the slip planes define a girdle if only one slip system is active (Fig. 1). Actual CPOs are, of course, more complicated for the reasons outlined above.

Purpose and analytical methods

The main purpose of this study is to semi-quantitatively assess strain geometry (the degree to which the strain deviated from plane strain toward flattening or constriction) using a large quartz CPO dataset. The same data are also used to assess active slip systems, CPO strength, and sense of shear. The samples are mostly quartzofeldspathic gneisses, quartzites, and quartz veins from the Western Gneiss region of Norway deformed at chiefly amphibolite-facies conditions. The CPO data were collected from X–Z thin sections (i.e. perpendicular to foliation and parallel to lineation) by electron back-scatter diffraction using a JEOL JSM-6300V digital SEM coupled with a HKL Nordlys EBSD camera and Channel 5 software. To create a CPO, the processed data were reduced to one point per grain, using a 15° misorientation to define grain boundaries. Pole figures of quartz [c] and <a> axes were created and contoured using the *PFch5* software (Mainprice 2005).

The modal proportions of quartz, feldspar, and "other" phases were determined from the area proportions of phases indexed during the EBSD measurements. These values were rounded to the nearest 5% to indicate their probable accuracy at the thin-section scale.

The orientations of the CPO eigenvectors (Ulrich & Mainprice 2005) define the orientation of the CPO skeleton. The asymmetry of the CPO skeleton with respect to the rock foliation and lineation was used to determine sense of shear (Behrmann & Platt 1982). The validity of this method hinges on the assumptions that i) the preferred glide plane is sufficiently close to the shear plane that the apparent sense of shear is not reversed, and ii) the strain that produced the CPO and the strain that produced the foliation were not sufficiently different to give the wrong sense of shear.

To assess CPO strength we use the *J* index (Bunge 1982) for the [c] axes and <a> axis fabrics. To determine strain geometry, we use the basic precepts implied by Lister et al. (1978) and expanded upon by Price (1985) (Fig. 1), inferring that the CPO skeleton reflects the strain geometry and the active slip systems. For example, deformation solely by prism <a> slip is expected to produce a [c] axis maximum during simple shear plane strain, a [c] axis girdle in the X–Y plane during flattening, and a [c] axis girdle in the Y–Z plane during constriction. In this view, the extent that a given [c] axis distribution falls between a maximum and a girdle can be used to determine the extent to which the strain was a mixture of plane strain and constriction. This determination can never be more than semi-quantitative for many reasons alluded to above, not the least of which are that slip systems and strains vary from grain to grain in rocks. Of particular relevance to amphibolite-facies deformation of quartz is that <a> pencil glide can occur along a combination of basal, prism, and rhomb planes; if these slip systems are active in concert, even plane strain may yield a CPO in a naturally deformed rock that is indistinguishable from the CPO expected for constriction-imposed slip on the basal <a> system or prism <a> system alone (Fig. 1) (Schmid & Casey 1986).

For a semi-quantitative measure of the degree to which a CPO defines a maximum or a girdle, we use *Pfch5* (Mainprice 2005) to calculate the *P*, *G*, and *R*

indices of the [c] axis distribution (Woodcock 1977; Vollmer 1990; Ulrich & Mainprice 2005). The magnitudes of the indices reflect how well the data define a point (*P*), girdle (*G*), or random (*R*) distribution. The *R* value serves as a measure of CPO strength, with *R* = 1 indicating the absence of a preferred orientation. These values can be displayed in a triangular "Vollmer" diagram (Abalos 1997) that has apices of *P*, *G*, and *R*. To remove the *R* component from the determination of the strain geometry, we calculate normalized point (P_n) and girdle (G_n) values:

$$P_n = P / (P + G)$$

$$G_n = G / (P + G) \quad \text{or} \quad G_n = 1 - P_n$$

In the case of basal <a> slip, a low P_n value indicates constriction (Fig. 1). A high P_n value is compatible with plane strain or flattening; the distinction between the two possibilities must be made on the basis to which the <a> axes define point maxima or a girdle. In the case of prism <a> slip, a high P_n value indicates plane strain. A low P_n value is compatible with constriction or flattening; the distinction between the two possibilities can be made by using the orientation of the [c] girdle with respect to the foliation: a girdle in the Y–Z plane indicates constriction and a girdle in the X–Y plane indicates flattening. In the case of prism [c] slip, a low P_n value indicates flattening. A high P_n value is compatible with constriction or plane strain; the distinction between the two possibilities must be made on the basis to which the <a> axes define point maxima or a girdle. In the case of "mixed <a>" slip (slip in the <a> direction along all planes, or pencil glide), the resulting CPOs cannot easily be deconstructed using P_n because the [c] axes effectively form one or more girdles regardless of whether the strain is plane or constrictional; flattening achieved by <a> slip along multiple planes will lead to an increased *R* component. Thus, only the P_n values for "prism <a>" CPOs are definitive of constriction vs. plane strain, and only when the orientation of the [c] axis girdle is considered. P_n values for "basal <a>" CPOs cannot distinguish between plane strain and flattening, and P_n for "prism [c]"

CPOs cannot differentiate constriction from plane strain. Simple P_n values for "mixed <a>" slip are not useful for assessing strain geometry.

The Western Gneiss Region ultrahigh-pressure terrane

The formation and exhumation of ultrahigh-pressure (UHP) rocks are important aspects of collisional orogenesis, and are intrinsic to a number of Earth processes, including the generation and collapse of mountain belts, crust–mantle material exchange, and the chemical refining of continental crust (Hacker 2007). The Western Gneiss Region (WGR) of Norway (Fig. 2), the root zone of the Scandinavian Caledonides, is the best-exposed giant UHP terrane on Earth and is thus a prime locale to study UHP processes. The bulk of the WGR consists of quartzofeldspathic Baltica basement gneiss overlain by minor crystalline and metasedimentary allochthons. High-pressure (HP) rocks cover 60,000 km^2, and UHP rocks, defined by the presence or absence of coesite, crop out in three antiformal domains along the coast (Hacker 2007). Peak metamorphic temperatures increase from ~600°C in the southeast to 800°C in the northwest (Fig. 2) (Griffin et al. 1985; Kylander-Clark et al. 2008). Subduction of the WGR was underway by 420 Ma and exhumation to mid-crustal levels was complete by 400–380 Ma (Kylander-Clark et al. 2007; Walsh et al. 2007).

Aspects of the exhumation history of the WGR that are not well understood include the spatial and temporal variations in: i) the sense of shear, ii) the magnitude of strain, and iii) the geometry of strain. The bulk of the exhumation-related fabrics are associated with E–W amphibolite-facies stretching, although older fabrics (including granulite and eclogite facies) are locally preserved (Terry & Robinson 2003, 2004). The principal structure responsible for exhumation of the WGR through crustal depths is the Nordfjord–Sogn Detachment Zone (Fig. 2) (Johnston et al. 2007a). This zone is characterized by amphibolite- to greenschist-facies asymmetric

structures that indicate top-W, normal-sense shear within the allochthons; it is well developed within the lower few km of the allochthons, but fades rapidly into the underlying crystalline basement (Andersen et al. 1994; Labrousse et al. 2002; Hacker et al. 2003; Johnston et al. 2007a; Young 2005). A top-E, amphibolite-facies high-strain zone occurs along the eastern edge of the crystalline basement.

Assessing the strain geometry of the WGR is important for understanding how the WGR was exhumed. Andersen et al. (1991) suggested that the WGR might contain constrictional fabrics formed as the buoyant continental crust tore loose from its sinking lithospheric root; Terry & Robinson (2003, 2004) described eclogite- and amphibolite-facies structures compatible with this. Andersen & Jamtveit (1990) reported symmetrical structures indicating eclogite- and amphibolite-facies coaxial deformation. Krabbendam & Wain (1997) observed L fabrics in augen gneiss and lineation-parallel folds in layered gneiss and concluded that the WGR experienced constrictional E–W extension, N–S shortening and vertical thinning during amphibolite-facies metamorphism. Walsh & Hacker (2004) noted that if the ascent of the WGR was arrested at the Moho because of neutral buoyancy it might have undergone large-scale flattening.

Data

One-hundred-and-one quartz-bearing rock sample from the WGR were included in this study: 64 samples newly analyzed and 37 from previous studies (Fig. 2, Appendix 1). Because previous studies generally focused on small areas, this study made an effort to broaden the spatial distribution of the samples; the result, however (Fig. 2), is still quite uneven, and this should be borne in mind when interpreting the dataset. The rocks are chiefly quartzofeldspathic gneisses, quartzites, and veins, with a few anorthosites, granulites and eclogites. Minerals present in the gneisses include quartz, plagioclase, K-feldspar, garnet, biotite, muscovite, chlorite, hornblende,

orthopyroxene, epidote, zoisite, sphene and kyanite. Most samples contain simply quartz ± feldspar ± mica. At some localities, suites of different rock types (quartzite vs. anorthosite vs. gneiss, or eclogite vs. quartzofeldspathic gneiss) were measured to assess the effect of rock type on the CPO recorded. At other localities, veins were measured separately from the host rocks for the same reason.

Optical microstructures of samples

Optically visible sample microstructures are summarized in Appendix 1 and Figure 3. The bulk of the samples display microstructures typical of Regime 3 deformation/recrystallization conditions —dentate grain boundaries, a modest range of grain sizes, island grains, and an absence of core-and-mantle microstructures— implying a mix of subgrain-rotation and grain-boundary migration recrystallization (Hirth & Tullis 1992; Stipp et al. 2002). Fewer samples show characteristics of Regime 2: ribbon grains, core-and-mantle microstructures, and deformation lamellae (Fig. 3). The amount of quartz in some samples is so low, 20–30%, that the grains were likely pinned by their neighbors and did not undergo pure dislocation creep.

Active slip systems

Most samples show strong lattice preferred orientations with multiples of uniform distribution (m.u.d.) of 3 or more; a few have m.u.d. >20 (Fig. 4). About half the samples have CPOs with a [c] axis maximum subparallel to the Y strain direction, compatible with prism <a> slip. About two dozen samples have CPOs with a [c] axis girdle subperpendicular to the X strain direction, evocative of <a> slip on multiple planes (i.e., pencil glide). Both of these types of CPO are distributed evenly across the study area (Fig. 5). Another eight samples have CPOs with a [c] axis maximum subparallel to X, implying prism [c] slip. These samples are all from a relatively small area around the UHP domains in the western part of the study area; some of

them are eclogites, others are veins associated with eclogites, and others are nearby gneisses. The two granulite-facies samples have obscure CPOs. About ten samples have CPOs with a [c] axis maximum subparallel to Z, suggesting basal <a> slip; these samples are widely scattered, but form a small cluster in the center of the study area (Fig. 5). The bulk of the samples thus experienced slip on systems typical of amphibolite-facies deformation; the few basal <a> slip and prism [c] slip CPOs imply greenschist-facies and granulite- or eclogite-facies deformation, respectively.

Age of the CPOs and microstructures

Several lines of evidence indicate that the bulk of the quartz CPOs and microstructures reported in this study formed during the amphibolite-facies exhumation of the WGR that postdated the UHP event. 1) In the WGR, the amphibolite-facies structures overprint local eclogite-facies structures (typically forming fractures, strain shadows, and shear zones), indicating that they are younger. 2) Quartz grains within the three UHP domains are presumed to be pseudomorphs after coesite, and therefore may have had a random orientation upon formation (Hacker & Peacock 1995; Lenze & Stöckhert 2007). 3) Several samples (particularly quartz veins P6824C2, K7711E2, and E9820M9) have strong CPOs that are not coaxial with respect to the rock foliation, suggesting that the quartz microstructure is younger than the foliation. 4) Most samples exhibit undulatory extinction; if that undulatory extinction had developed during an earlier deformation it would have been annealed during a static amphibolite-facies event. Specific exceptions to this conclusion that the bulk of the CPOs reflect amphibolite-facies exhumation, are the granulite-facies and eclogite-facies samples CPOs, which are relicts of earlier deformation.

Sense of shear

Sixty-four of the [c] and <a> axis CPOs are asymmetric with respect to the rock foliation; 21 are symmetrical, and 16 are indeterminate. The asymmetric CPOs, implying noncoaxial deformation, and the symmetric CPOs, implying coaxial deformation, show spatial distributions (Fig. 5). The CPOs of samples around the Nordfjord–Sogn Detachment Zone in the west are almost uniformly indicative of top-W amphibolite-facies shearing (Young 2005; Johnston et al. 2007b). The central part of the study area is characterized by a mix of symmetric CPOs that imply coaxial sample-scale deformation, and subequal numbers of asymmetric CPOs that imply top-W and top-E sample-scale shearing. Together, these CPOs imply that the central domain underwent broadly coaxial deformation. The inferred slip systems of these samples are compatible with amphibolite-facies deformation. The central domain and the Nordfjord–Sogn Detachment Zone are separated by a transitional domain characterized by a mixture of CPOs suggesting top-W and coaxial shearing from amphibolite facies down to greenschist facies. Within this domain is a smaller domain of CPOs compatible with a mix of top-W and top-E shearing during eclogite-or granulite-facies deformation. Along the eastern edge of the WGR is a fourth domain with CPOs implying top-E shearing, again compatible with field observations.

CPO strength

The CPO strength, as determined by $J_{[c]}$, $J_{<a>}$ or $1–R$, shows modest spatial variation (Fig. 6). Samples around the high-strain Nordfjord–Sogn Detachment Zone and from an area in the eastern part of the study area have strong CPOs, whereas samples everywhere else have weaker CPOs.

Strain geometry

The distributions of the *PGR* data for the different CPOs (Fig. 4) imply that the strain that produced the CPOs was a mix of plane strain and constriction, with minimal flattening. Most of the CPOs that are compatible with basal <a> slip have relatively high *R* values that render their interpretation suspect. Of the five samples with low *R* values, one, J2803M, has a [c] axis girdle that might indicate constriction. The remaining low-*R* samples have CPOs compatible with plane strain (e.g., P6822B1) or flattening (e.g., J2813D). The CPOs that are compatible with prism <a> slip indicate a mix of plane strain and constriction, with the former dominant; none are suggestive of flattening. The CPOs that are compatible with "mixed <a>" slip are, *de facto*, all compatible with constriction and plane strain, but—as noted above—P_n cannot distinguish between those two possibilities. The CPOs that are compatible with prism [c] slip samples are suggestive of either plane strain (e.g., Y1706B) or constriction (e.g., K7717A).

Figure 7 shows the spatial distribution of the P_n data for the "prism <a>" slip samples; samples with high *R* values or obscure CPOs were excluded (see Appendix 1). Adding the "basal <a>" slip and 1–P_n for the "prism [c]" samples does not affect the general pattern. The greatest constrictional component (low Pn values) is recorded in the center of the study area (Fig. 7).

Rock-type comparisons

At six locations, different types of rock were measured to assess how the presence of minerals other than quartz affected the CPOs. A quartzite and a gneiss sample at E1606L record CPOs that look similar despite the percentage of quartz varying by a factor of two (Appendix 1). A quartzite and a vein sample at K7710R have almost identical amounts of quartz and recorded essentially identical CPOs. Three K7711E samples, a gneiss, a quartzite and a vein, have partial to complete [c] axis girdles subperpendicular to X; the CPO in the quartzite (K7711E3) is the most

straightforward, and the CPO in the gneiss (K7711E1 is the most obscure. The three eclogite-facies samples from P6807F have obscure, but similar, CPOs. The two gneiss samples from P6824C have similar CPOs suggesting prism <a> or mixed <a> slip, whereas the vein sample (P6824C2) has a clearly defined prism <a> CPO.

Discussion

Implications for deformation of the Western Gneiss Region

The quartz CPO data presented above provide useful information regarding the exhumation of the WGR. Although most of the CPOs imply amphibolite-facies mixed <a> slip and prism <a> slip, the presence of CPOs in a minority of samples suggesting prism [c] slip indicates that vestiges of hotter deformation remain. The sense-of-shear interpretations imply that the hottest deformation (recorded by prism [c] CPOs) was coaxial at a large scale (a mixture of top-W and top-E), compatible with the interpretation of field structures by Andersen & Jamtveit (1990). The rest of the sense-of-shear interpretations show a clear east-to-west transition: an eastern domain with top-E amphibolite-facies deformation, a central coaxial domain that is mostly amphibolite-facies, but locally greenschist facies, and strong top-W, normal-sense shearing along the Nordfjord–Sogn Detachment Zone. The extent to which the top-W deformation within the Nordfjord–Sogn Detachment Zone extends downward to deeper structural levels within the crystalline basement—as shown by the new CPOs—was not previously recognized. The eastern domain of top-E shearing is associated with emplacement of the allochthons over the basement; that this deformation is chiefly amphibolite-facies was not previously known.

As noted above, numerous factors influence CPO strength, including the particular slip systems that are active, the activity of other deformation mechanisms, the rate of recrystallization, the presence of other phases, and variations in strain

path, including strain magnitude. Two domains in the study area, the Nordfjord–Sogn Detachment Zone and the eastern margin of the crystalline basement, have outcrop features—reduced grain size, stronger foliations, and strong fabric asymmetry—indicating high strain magnitude. These two domains do indeed have strong CPOs locally (as measured by $J_{[c]}$ of quartz), implying that dislocation creep of quartz was a significant deformation mechanism.

The strain geometries calculated in this study from quartz CPOs are a mix of plane strain and constriction, with minimal evidence of a flattening component. Because of the relatively low strains necessary to reset quartz CPOs, these are true constrictional strains and not "apparent" constriction that might result from, for example, the superposition of orthogonal flattening strains. The evidence of widespread true constriction is consistent with the suggestions of Krabbendam & Wain (1997) that constrictional E–W extension, vertical thinning and N–S shortening occurred throughout the WGR during the late-Caledonian amphibolite-facies metamorphism. It is possible that other phases and/or rock types not measured in this study accommodated other strain geometries, including flattening.

Implications for interpreting quartz CPOs

This study demonstrates that qualitative assessment of strain geometry is possible using quartz CPOs. There are three actions that would enable *quantitative* assessment of strain geometry. 1) Viscoplastic modeling of quartz CPOs (Wenk et al. 1989) must be expanded to include <a> axes and conducted to sufficiently high strains to produce CPOs with strengths similar to natural CPOs. 2) A means of assessing the degree to which <a> axes deviate between maxima, girdles, and random must be devised. 3) The initial work of Price (1985), comparing CPOs with measured strain geometries, must be expanded to complete crystal orientations using EBSD.

Although quartz CPOs with Type-I and Type-II (Lister 1977) [c] axis girdles are common in the literature, and are indeed typical of some amphibolite-facies terranes (e.g. Lister & Dornsiepen 1982; Schmid & Casey 1986; Law 1990; Xypolias & Koukouvelas 2001; Llana-Fúnez 2002), they are rare components of this dataset, implying a difference in deformation or that EBSD-generated CPOs look different or are different from U-stage generated CPOs.

Conclusions

Slip systems, sense of shear, CPO strength, and strain geometry across the ultrahigh-pressure Western Gneiss Region of Norway were assessed using CPOs measured with electron back-scatter diffraction. CPOs with [c] axis maxima subparallel to X indicate local preservation of eclogite- or granulite-facies prism [c] slip. The bulk of the CPOs, however, have [c] axis maxima subparallel to Y or great-circle girdles subperpendicular to X, implying a dominance of prism <a> slip and mixed <a> slip; this is the characteristic amphibolite-facies deformation of the Western Gneiss Region. There are few Type-I and Type-II girdles, in contrast to other studies. Asymmetric and strong CPOs characterize the high-strain, top-W, normal-sense Nordfjord–Sogn Detachment Zone and a top-E domain along the eastern margin of the crystalline basement. The [c] axis distributions of the CPOs suggest that the strain was characterized by a mix of plane strain and constriction and minimal flattening; this supports earlier field-based studies.

Acknowledgements

Funded by NSF EAR-0510453. Dedicated to Martin Casey for his kindness and pioneering work on CPO measurement and interpretation. Extensive and thoughtful reviews by Geoffrey Lloyd and Paris Xypolias, and discussions with Phil Gans and Jeffrey Lee are gratefully acknowledged.

Figure Captions

Figure 1. CPOs and normalized point (P_n) and girdle (G_n) indices expected from various quartz slip systems subjected to different strain geometries. In each stereonet, foliation (Sf) is horizontal, shear/cisaillement (C) planes are inclined, and lineation is at the intersection of the foliation with the primitive (i.e., E–W).

Figure 2. The Western Gneiss Region of Norway consists of a crystalline basement overlain by allochthons emplaced toward the southeast. Major features include the ultrahigh-pressure (UHP) domains, the top-W Nordfjord–Sogn Detachment Zone and the top-E shear zone along the eastern edge of the crystalline basement. Peak metamorphic temperatures increase toward the northwest (Kylander-Clark et al. 2008); the CPOs reported here reflect either these or lower temperatures.

Figure 3. Representative microstructures. Optical microstructures (left) are indicative of quartz deformation Regime 2 (a few samples) or 3 (most samples); cross-polarized light. EBSD map colored by one-point-per-grain quartz crystal orientations shown in inset [c] axis stereonet. **(a)** Quartz vein P6807F7 showing weak undulatory extinction, weak sub-grain formation, and fairly straight grain boundaries indicative of quartz deformation Regime 3. **(b)** Quartz vein in eclogite K7717A2 showing weak undulatory extinction, modest sub-grain formation, and straight grain boundaries indicative of Regime 3. **(c)** Gneiss sample R9823F9 composed of bands of quartz and plagioclase. Regime 3. **(d)** Gneiss sample P6821D1 with quartz-rich zones surrounded by fine-grained symplectites. Grain boundaries are dentate. Regime 3. **(e)** Gneiss sample P6803A2 with strong undulatory extinction, strong sub-grain formation, and dentate grain boundaries indicative of sub-grain rotation recrystallization

(Regime 2). **(f)** Quartz-rich ultramylonite J3701E3 with highly stretched quartz grains and feldspar porphyroclasts. Regime 2.

Figure 4. Representative quartz CPOs and calculated P, G, R values. Upper hemisphere projections in which the <a> axes have been collapsed using 622 symmetry. CPOs for other 'J' and 'Y' samples can be found in Johnston et al. (2007b) and Young (2005), respectively. **(a)** CPOs attributable to basal <a> glide have characteristics compatible with plane strain or flattening (4 samples) and constriction (1 sample); another seven samples have more obscure CPOs with high *R* values. **(b)** CPOs attributable to prism <a> glide have characteristics compatible with a mix of plane strain and constriction, with the former dominant; none are compatible flattening. **(c)** CPOs attributable to "mixed <a>' slip are compatible with constriction and plane strain. **(d)** CPOs attributable to prism [c] slip are compatible with either plane strain (e.g., Y1706B) or constriction (e.g., K7717A).

Figure 5. Slip systems and shear sense inferred from CPOs show distinct domains: top-W prism <a> slip along the Nordfjord–Sogn Detachment Zone, mixed prism [c] slip in the west near the southernmost UHP domain, and a transition to top-E shear farther east. Dashed arrows indicate less robust data.

Figure 6. As measured by $J_{[c]}$ value ($J_{<a>}$ is nearly identical and $1–R$ is similar), CPOs are strongest along the Nordfjord-Sogn Detachment Zone and within the top-E domain in the east. Contoured using the Matlab griddata(cubic) routine.

Figure 7. The constrictional component inferred from CPOs using P_n is weakest in the south(east) and strongest in the north(west). Only samples with P_n values listed in Appendix 1 were used (i.e., samples with large *R* values or obscure CPOs were excluded). Contoured using the *Matlab* griddata(cubic) routine.

References Cited

Abalos, B. 1997. Omphacite fabric variation in the Cabo Ortegal Eclogite (NW Spain); relationships with strain symmetry during high-pressure deformation. *Journal of Structural Geology*, **19**, 621-637.

Andersen, T.B. & Jamtveit, B. 1990. Uplift of deep crust during orogenic extensional collapse: a model based on field studies in the Sogn–Sunnfjord region of western Norway. *Tectonics*, **9**, 1097-1111.

Andersen, T.B., Jamtveit, B., Dewey, J.F. & Swensson, E. 1991. Subduction and exhumation of continental crust: major mechanism during continent-continent collision and orogenic extensional collapse, a model based on the south Caledonides. *Terra Nova*, **3**, 303-310.

Andersen, T.B., Osmundsen, P.T. & Jolivet, L. 1994. Deep crustal fabrics and a model for the extensional collapse of the southwest Norwegian Caledonides. *Journal of Structural Geology*, **16**, 1191-1203.

Baëta, R.D. &Ashbee, K.H.G. 1969. Slip systems in quartz: I. Experiments, *American Mineralogist*, **54**, 1551–1573.

Bascou, J., Tommasi, A. &Mainprice, D. 2002. Plastic deformation and development of clinopyroxene lattice preferred orientations in eclogites. *Journal of Structural Geology*, **24**, 1357-1368.

Behrmann, J.H. & Platt, J.P. 1982. Sense of nappe emplacement from quartz c-axis fabrics: an example from the Betic Cordilleras (Spain). *Earth and Planetary Science Letters*, **59**, 208–215.

Blacic, J.D. 1975. Plastic-deformation mechanisms in quartz; the effect of water. *Tectonophysics*, **27**, 271-294.

Blacic, J.D. & Christie, J.M. 1984. Plasticity and hydrolytic weakening of quartz single crystals. *Journal of Geophysical Research*, **89**, 4223–4239.

Blumenfeld, P., Mainprice, D. & Bouchez, J.-L. 1986. C-slip in quartz from subsolidus deformed granite. *Tectonophysics*, **127**, 97-115.

Bouchez, J.-L. 1977. Plastic deformation of quartzites at low temperature in an area of natural strain gradient. *Tectonophysics*, **39**, 25–50.

Bouchez, J.-L., Lister, G.S. & Nicolas, A. 1983. Fabric asymmetry and shear sense in movement zones, *Geologische Rundschau*, **72**, 410–419.

Bunge, H.-J. 1977. *Texture Analysis in Materials Science*, 593 pp., Butterworths, London.

Carreras, J., Estrada, A. & White, S. 1977. The effects of folding on the c-axis fabrics of a quartz mylonite. *Tectonophysics*, **39**, 3-24.

Casey, M. & McGrew, A.J. 1999. One-dimensional kinematic model of preferred orientation development. *Tectonophysics*, **303**, 131-140.

Christie, J.M., Griggs, D.T. & Carter, N.L. 1964. Experimental evidence of basal slip in quartz. *Journal of Geology*, **72**, 734-756.

Dell'Angelo, L.N. & Tullis, J. 1989. Fabric development in experimentally sheared quartzites. *Tectonophysics*, **169,** 1–22.

Griffin, W.L., Austrheim, H., Brastad, K., Bryhni, I., Krill, A.G., Krogh, E.J., Mørk, M.B.E., Qvale, H. & Torudbakken, B. 1985. High-pressure metamorphism in the Scandinavian Caledonides. *In:* Gee, D.G. & Sturt, B.A. (eds) *The Caledonide Orogen; Scandinavia and related areas.* John Wiley & Sons, Chichester, 783-801..

Hacker, B.R. 2007. Ascent of the ultrahigh-pressure Western Gneiss Region, Norway. In: Cloos, M., Carlson, W.D., Gilbert, M.C., Liou, J.G. & Sorenson, S.S. (eds) *Convergent Margin Terranes and Associated Regions: A Tribute to W.G. Ernst, Geological Society of America Special Paper*, XX, 171-184.

Hacker, B.R., Andersen, T.B., Root, D.B., Mehl, L., Mattinson, J.M. & Wooden, J.L. 2003. Exhumation of high-pressure rocks beneath the Solund Basin, Western Gneiss Region of Norway. *Journal of Metamorphic Geology*, **21,** 613–629.

Hacker, B.R. &Peacock, S.M. 1995. Creation, preservation, and exhumation of coesite-bearing, ultrahigh-pressure metamorphic rocks. In: Coleman, R.G. & Wang, X. (eds) *Ultrahigh Pressure Metamorphism.* Cambridge University Press,159–181..

Heilbronner, R. and Tullis, J. 2006. Evolution of c-axis pole figures and grain size during dynamic recrystallization: results from experimentally sheared quartzite. Journal of Geophysical Research, 111, B10202, doi:10.1029/2005JB004194.

Hirth, G. & Tullis, J. 1992. Dislocation creep regimes in quartz aggregates. *Journal of Structural Geology*, **14**, 145–159.

Johnston, S., Hacker, B.R. & Andersen, T.B. 2007a. Exhuming Norwegian ultrahigh-pressure rocks: Overprinting extensional structures and the role of the Nordfjord-Sogn Detachment Zone. *Tectonics*, **26**, TC5001, doi:10.1029/2005TC001933.

Johnston, S., Hacker, B.R. & Ducea, M.N. 2007b. Exhumation of ultrahigh-pressure rocks beneath the Hornelen segment of the Nordfjord-Sogn Detachment Zone, western Norway. *Geological Society of America Bulletin*, **119**, 1232-1248,.

Knipe, R.J. & Law, R.D. 1987. The influence of crystallographic orientation and grain-boundary migration on microstructural and textural evolution in an SC mylonite. *Tectonophysics*, **135**, 153–169.

Krabbendam, M. Wain, A. 1997. Late-Caledonian structures, differential retrogression and structural position of (ultra) high pressure rocks in the Nordfjord–Stadlandet area, Western Gneiss Region. *Norges Geologiske Undersøkelse Bulletin*, **432**, 127-139.

Kylander-Clark, A.R.C., Hacker, B.R., Johnson, C.M., Beard, B.L., Mahlen, N.J. & Lapen, T.J. 2007. Timing of multi-stage metamorphism during ultrahigh-

pressure continental subduction and exhumation: Lu/Hf and Sm/Nd geochronology in western Norway. *Chemical Geology*, **232**, 137-154.

Kylander-Clark, A.R.C., Hacker, B.R. & Mattinson, J.M. 2008. Slow exhumation of UHP terranes: Titanite and rutile ages of the Western Gneiss Region, Norway. *Earth and Planetary Science Letters*, **272**, 531-540.

Labrousse, L., Jolivet, L., Agard, P., Hébert, R. & Andersen, T.B. 2002. Crustal-scale boudinage and migmatization of gneiss during their exhumation in the UHP Province of Western Norway. *Terra Nova*, **14**, 263-270.

Law, R.D. 1986. Relationships between strain and quartz crystallographic fabrics in the Roche Maurice quartzites of Plougastel, western Brittany. *Journal of Structural Geology*, **8**, 493–515.

Law, R.D. 1990. Crystallographic fabrics: a selective review of their application to research in structural geology. *In*: Knipe, R.J. & Rutter, E.H. (eds) *Deformation Mechanisms, Rheology and Tectonics*. Geological Society, London, Special Publications, **54**, 335-352.

Lenze, A. & Stöckhert, B. 2007. Microfabrics of UHP metamorphic granites in the Dora Maira Massif, western Alps – no evidence of deformation at great depth. *Journal of Metamorphic Geology*, **25**, 461-475.

Linker, M.F., Kirby, S.H., Ord, A. & Christie, J.M. 1984. Effects of compression direction on plasticity and rheology of hydrolytically weakened synthetic quartz at atmospheric pressure. *Journal of Geophysical Research*, **89**, 4241-4255.

Lister, G.S. 1977. Discussion; crossed-girdle c-axis fabrics in quartzites plastically deformed by plane strain and progressive simple shear. *Tectonophysics*, **39**, 51-54.

Lister, G.S. 1982. A vorticity equation for lattice reorientation during plastic deformation. *Tectonophysics*, **82**, 351-366.

Lister, G.S. & Dornsiepen, U.F. 1982. Fabric transitions in the Saxony granulite terrain. *Journal of Structural Geology*, **11**, 65–94.

Lister, G.S. & Hobbs, B.E. 1980. The simulation of fabric development during plastic deformation and its application to quartzite: the influence of deformation history. *Journal of Structural Geology*, **2**, 355–370.

Lister, G.S., Paterson, M. & Hobbs, B.E. 1978. The simulation of fabric development during plastic deformation and its application to quartzite: the model. *Tectonophysics*, **45**, 107–158.

Llana-Fúnez, S. 2002. Quartz C-axis texture mapping of a Variscan regional foliation (Malpica-Tui Unit, NW Spain). *Journal of Structural Geology*, **24**, 1299-1312.

Lloyd, G.E. 2004. Microstructural evolution in a mylonitic quartz simple shear zone; the significant roles of Dauphiné twinning and misorientation. In: Alsop, G.I., Holdsworth, R.E., McCaffrey, K. & Hand, M. (eds) *Transports and Flow Processes in Shear Zones. Geological Society*, London, Special Publications, **224**, 39-224.

Mainprice, D. 2005. Pfch5 [Computer software], edited by ftp://www.gm.univ-montp2.fr/mainprice//CareWare_Unicef_Programs/.

Marjoribanks, R.W. 1976. The relation between microfabric and strain in a progressively deformed quartzite sequence from central Australia. *Tectonophysics*, **32**, 269-293.

Miller, D.M.& Christie, J.M. 1981. Comparison of quartz microfabric with strain in recrystallized quartzite. *Journal of Structural Geology*, **3**, 129-141.

Price, G.P. 1985. Preferred orientations in quartzites. In: Wenk, H.R. (ed) *Preferred Orientation in Deformed Metals and Rocks: An Introduction to Modern Texture Analysis*. Academic Press, Inc., Orlando, 385–406.

Schmid, S.M. & Casey, M. 1986. Complete fabric analysis of some commonly observed quartz c-axis patterns. *Geophysical Monograph*, **36**, 263–286.

Stipp, M., Stünitz, H., Heilbronner, R. & Schmid, S. 2002. Dynamic recrystallization of quartz: correlation between natural and experimental conditions. In: De Meer, S., Drury, M.R., De Bresser, J.H.P. & Pennock, G.M. (eds) *Deformation Mechanisms, Rheology and Tectonics: Current Status and Future Perspectives.* Geological Society, London, Special Publications, **200**,171-190.

Taylor, G.I. 1938. Plastic strain in metals. *Journal Institute of Metals*, **62**, 307-324.

Terry, M.P. & Robinson, P. 2003. Evolution of amphibolite-facies structural features and boundary conditions for deformation during exhumation of high- and ultrahigh-pressure rocks, Nordøyane, Western Gneiss Region, Norway. *Tectonics*, **22**, 1036 10.1029/2001TC001349.

Terry, M.P. & Robinson, P. 2004. Geometry of eclogite-facies structural features: Implications for production and exhumation of UHP and HP rocks, Western Gneiss Region, Norway. *Tectonics*, **23**, doi: 10.1029/2002TC001401.

Tullis, J., Christie, J.M. & Griggs, D.T. 1973. Microstructure and preferred orientations of experimentally deformed quartzites. *Geological Society of America Bulletin*, **84**, 297–314.

Ulrich, S. & Mainprice, D. 2005. Does cation ordering in omphacite influence development of lattice-preferred orientation? *Journal of Structural Geology*, **27**, 419-431.

Vollmer, F.W. 1990. An application of eigenvalue methods to structural domain analysis. *Geological Society of America Bulletin*, **102**, 786-791.

Walsh, E.O. & Hacker, B.R. 2004. The fate of subducted continental margins: Two-stage exhumation of the high-pressure to ultrahigh-pressure Western Gneiss complex, Norway. *Journal of Metamorphic Geology*, **22,** 671-689.

Walsh, E.O., Hacker, B.R., Grove, M., Gans, P.B. & Gehrels, G. 2007. Timing the exhumation of (ultra)high-pressure rocks across the Western Gneiss Region, Norway. *Geological Society of America Bulletin*, **119**, 289-301.

Wenk, H.-R., Canova, G., Molinari, A. & and Kocks, U.F. 1989. Viscoplastic modeling of texture development in quartzite. *Journal of Geophysical Research*, **94,** 17895–17906.

Wenk, H.R. & Christie, J.M. 1991. Comments on the interpretation of deformation textures in rocks. *Journal of Structural Geology*, **13**, 1091-1110.

Woodcock, N.H. 1977. Specification of fabric shapes using an eigenvalue method. *Geological Society of America Bulletin*, **88**, 1231-1236.

Xypolias, P. & Koukouvelas, I.K. 2001. Kinematic vorticity and strain rate patterns associated with ductile extrusion in the Chelmos shear zone (external Hellenides, Greece). *Tectonophysics*, **338,** 59-77.

Young, D. 2005. *Amphibolite to Ultrahigh-Pressure Transition in Western Norway*. Unpublished Ph.D. thesis, University of California, Santa Barbara.

Appendix 1. Part 1: EBSD data.

	rock	UTM	UTM	Foliation Lineation		J [c]	J <a>	Dominant slip	P	G	R	Pn	Shear Sense
E9730H1	gneiss	501347	6885005	129/54	167/41	2.0	1.3	prism <a>	0.23	0.41	0.36	0.36	
E9801i1	quartzite	475357	6904137	070/10	105/01	4.4	1.8	prism <a>	0.60	0.20	0.20	0.75	top E(?)
E9801O1	quartzite	473503	6896805	177/59	096/09	2.7	1.5	prism <a>	0.40	0.32	0.28	0.56	dextral
E9804H	gneiss	418722	6913211	162/55	241/05	1.7	1.2	<a> slip?	0.18	0.41	0.41	0.30	top W
E9805B5	vein	421351	6897587	142/40	061/30	2.0	1.3	prism <a>	0.82	0.14	0.04	0.85	symmetrical
E9805M	gneiss	412438	6908815	138/35	122/35	2.7	1.4	prism <a>	0.04	0.38	0.59	0.09	symmetrical
E9805N	gneiss	412319	6908500	144/35	078/15	1.6	1.2	prism+rhomb <a>	0.21	0.20	0.58	0.52	top E
E9809C6	gneiss	391713	6890278	082/25	120/25	1.2	1.1	basal <a>	0.08	0.12	0.79		top W
E9810E	quartzite	360714	6857805	302/07	247/07	4.0	1.7	prism <a>	0.57	0.21	0.22	0.73	symmetrical
E9816B6	gneiss	412000	687890	045/40	100/24	2.4	1.4	basal <a>	0.33	0.29	0.38	0.54	top W
E9816E	gneiss	431450	6875648	269/12	114/11	1.4	1.1	<a> slip	0.08	0.23	0.69		top W
E9816F	gneiss	433871	6875328	114/50	054/25	1.7	1.2	basal <a>	0.18	0.25	0.56	0.42	sinistral
E9818B	gneiss	438451	6863002	028/45	078/35	1.8	1.2	<a> slip	0.11	0.39	0.50	0.22	top W
E9818F2	gneiss	428332	6875575	080 46	112/40	3.5	1.6	prism <a>	0.47	0.23	0.30	0.67	top E(?)
E9819A	gneiss	427527	6877800	050/43	090/34	4.3	1.7	prism <a>	0.54	0.23	0.23	0.70	top W(?)
E9820M9	vein	385400	686740	050/50	075/19	6.8	2.8	prism <a>	0.56	0.25	0.19	0.69	
E1606L5	quartzite	473777	6878900	147/85	069/24	2.4	1.5	<a> slip>	0.21	0.58	0.21	0.27	dextral
E1606L6	gneiss	473777	6878900	090/70	090/46	2.0	1.3	<a> slip	0.13	0.55	0.33	0.19	symmetrical
E1608G1	gneiss	408854	6868422	005/74	088/38	3.7	1.9	basal <a>	0.15	0.39	0.45		
E1612C9	gneiss	342678	6899395	137/10	177/05	1.9	1.2	<a> slip	0.16	0.27	0.58	0.37	top N
E1613P	gneiss	410809	6901325	082/16		1.3	1.1	<a> slip	0.02	0.17	0.81		
E1614A7	granulite	421807	6897223	045/36	060/15	10.1	2.8	?	0.82	0.14	0.04		
E1627E	gneiss	514xxx	6860xxx	208/30	276/13	1.4	1.1	<a> slip	0.10	0.46	0.44	0.18	symmetrical
H1604I3	gneiss	5454xx	70225xx	350/84	078/24	1.3	1.1	<a> slip	0.07	0.32	0.61		dextral
J2801C	quartzite	336970	6842464	186/61	277/15	1.5	1.1	<a> slip	0.06	0.49	0.45	0.11	sinistral
J2802H1	quartzite	335811	6848823	349/29	265/05	4.1	1.7	prism <a>	0.60	0.21	0.20	0.74	top W
J2802L	quartzite	333726	6848065	186/80	270/10	4.2	1.7	prism <a>	0.59	0.26	0.15	0.70	sinistral
J2802S2	quartzite	331352	6845675	210/40	215/38	1.7	1.2	<a> slip	0.09	0.57	0.34	0.14	top W
J2803M	quartzite	325790	6036350	347/26	286/12	2.2	1.3	basal <a>	0.18	0.59	0.23	0.23	top W
J2804L2	gneiss	323903	6830723	198/26	287/02	2.2	1.3	prism <a>	0.39	0.26	0.35	0.60	top E
J2804L31	quartzite	323903	6830723	198/26	287/02	6.6	2.2	prism <a>	0.77	0.13	0.10	0.86	top W(?)
J2805S	quartzite	294817	6836146	015/69	092/28	2.6	1.3	prism <a>	0.30	0.45	0.25	0.40	sinistral
J2806A2	quartzite	318548	6842979	304/25	291/20	2.3	1.3	prism <a>	0.37	0.35	0.29	0.51	top W
J2812A	quartzite	312165	6835751	347/34	299/22	1.9	1.2	prism <a>	0.15	0.56	0.29	0.22	top W
J2813D	quartzite	330516	6841848	201/73	282/28	2.3	1.3	basal <a>	0.36	0.33	0.31	0.52	sinistral

J2818J	quartzite	341050	6837880	342/30	284/19	2.0	1.3	<a> slip	0.18	0.51	0.31	0.26	top E
J2819D	quartzite	332184	6835836	005/17	284/05	2.6	1.3	prism <a>	0.23	0.53	0.24	0.30	top E
J3628B	quartzite	329391	6842480	000/82	275/30	1.9	1.2	prism <a>	0.27	0.31	0.42	0.46	sinistral
J3630D	quartzite	322608	6836411	308/09	277/08	2.9	1.4	prism <a>	0.39	0.33	0.27	0.54	top W
J3701E3	Ultramylon	325260	6833545	313/09	292/08	3.2	1.5	prism <a>	0.20	0.65	0.15	0.24	top W
J3701E4	Ultramylon	325260	6833545	252/28	294/22	2.1	1.3	<a> slip	0.32	0.30	0.38	0.52	top W
J3705H	quartzite	342090	6846709	004/70	271/10	2.2	1.4	prism <a>	0.32	0.30	0.38	0.52	sinistral
J5814C	gneiss	465986	6920669	070/40	070/40	4.1	1.8	prism <a>	0.51	0.23	0.26	0.69	top E(?)
J5814N2	gneiss	454500	6973000	335/85	065/06	1.4	1.1	<a> slip	0.10	0.34	0.55	0.24	symmetrical
J5815C	gneiss	392259	6963026	185/84	270/35	1.2	1.1	prism <a>	0.13	0.03	0.85		symmetrical
J5815E4	gneiss	398970	6970946	168/80	082/01	1.5	1.1	basal-prism <a>	0.12	0.37	0.52	0.24	sinistral
J5815F2	vein	394992	6977929	160/10	067/01	8.1	2.7	prism <a>	0.53	0.29	0.18	0.65	top W
J5816L2	quartzite	506601	6978402	267/73	210/62	3.2	1.5	basal <a>?	0.44	0.18	0.38	0.71	top N
K7708J	vein	527070	6928273	099/29	125/26	1.7	1.2	<a> slip	0.04	0.42	0.54	0.09	top E
K7709H6	quartzite	506173	6950741	344/24	080/05	3.2	1.5	prism <a>?	0.39	0.40	0.21	0.49	top E
K7710R1	vein	488814	6955139	145/05	105/05	7.1	2.7	prism <a>	0.73	0.16	0.11	0.82	top E
K7710R2	quartzite	488814	6955139	145/05	105/05	4.4	1.8	prism <a>	0.59	0.23	0.18	0.71	top E
K7710S	gneiss	488584	6955078	095/05	102/05	3.8	1.7	prism <a>	0.57	0.22	0.21	0.72	
K7711D	gneiss	495410	6960629	080/10	080/10	1.8	1.2	prism <a>	0.23	0.29	0.47	0.45	
K7711E1	gneiss	495414	6960662	155/15	096/12	1.6	1.2	prism <a>	0.17	0.22	0.62		
K7711E2	vein	495414	6960662	132/15	096/12	4.3	2.1	prism <a>?	0.44	0.39	0.17	0.53	
K7711E3	quartzite	495414	6960662	155/15	096/12	2.9	1.7	<a> slip	0.18	0.68	0.15	0.21	top E
K7711K	gneiss	499xxx	6979xxx	350/67	080 01	1.5	1.1	<a> slip	0.11	0.34	0.55	0.25	dextral
K7714A2	gneiss	329382	6913024	132/78	051/36	2.0	1.2	prism <a>	0.25	0.15	0.60	0.61	sinistral(?)
K7716A	gneiss	310706	6902585	120/24	110/19	1.7	1.2	<a> slip	0.22	0.03	0.75		
K7717A	vein in eclc	313814	6872804	145/60	230/15	5.5	1.7	prism [c]	0.54	0.19	0.27	0.74	sinistral
K7717G	granulite	292229	6883093	065/89	320/05	1.9	1.3	basal+rhomb<a>	0.21	0.39	0.40	0.35	dextral
K7719A	quartzite	427817	6893106	008/42	292/06	2.8	1.5	prism <a>?	0.50	0.08	0.42	0.87	top E(?)
K7721C	quartzite	481595	6903849	330/30	245/05	7.3	3.0	prism <a>	0.76	0.16	0.08	0.83	symmetrical
P6803A2	gneiss	440197	6840096	170/49	125/35	1.5	1.1	basal <a>?	0.12	0.37	0.51	0.25	symmetrical
P6807F7	vein in eclc	301660	6891370	020/55	108/20	8.1	1.7	prism [c]?	0.10	0.40	0.50		
P6807F8	vein	301660	6891370	035/50	110/15	2.2	1.3	<a> slip	0.33	0.29	0.38	0.53	dextral
P6807F9	eclogite	301660	6891370	120/20	132/15	2.2	1.4	prism [c]	0.29	0.13	0.58	0.69	top E
P6807G2	eclogite	302307	6891321	060/31	115/10	2.8	1.5	prism [c]?	0.14	0.41	0.45	0.25	
P6808A3	gneiss	491800	6858000	025/35	080/20	3.5	1.3	prism <a>	0.21	0.39	0.40	0.35	
P6809A3	gneiss	463565	6861331	132/40	094/39	2.7	1.4	prism <a>	0.48	0.11	0.41	0.81	symmetrical
P6821D1	gneiss	345700	6851400	166/56	100/18	1.7	1.2	<a> slip	0.12	0.37	0.51	0.25	dextral

P6822B1	gneiss	334890	6885870	117/75	047/50	3.0	1.6	basal <a>	0.43	0.31	0.26	0.58	symmetrical
P6824C1	gneiss	294809	6878942	010/42	075/20	1.4	1.1	prism <a>?	0.23	0.14	0.63	0.61	top W(?)
P6824C2	gneiss	292xxx	6883xxx	006/35	280/05	1.4	1.1	prism <a>	0.12	0.24	0.64		symmetrical
P6824C2	vein	292xxx	6883xxx	006/35	280/05	5.1	2.3	prism <a>	0.48	0.38	0.14	0.56	
P6826E1	gneiss	383482	6929460	071/11	089/11	2.0	1.2	basal <a>?	0.38	0.16	0.46	0.70	
8815G11	gneiss	319906	6907793	220/50	130/01	2.6	1.4	prism <a>	0.42	0.13	0.44	0.76	symmetrical
8829A2	gneiss	302350	6924950	None		1.2	1.0	basal <a>?	0.06	0.16	0.78		
8830B9	vein	328000	6920100	178/89	091/02	2.3	1.6	<a> slip	0.16	0.18	0.66		sinistral(?)
R8906B9	vein	325000	6921700	142/35	271/09	3.9	1.9	prism <a	0.39	0.20	0.41	0.67	top E
R9823F9	gneiss	336147	6911512	157/70	115/70	2.2	1.3	<a> slip	0.35	0.14	0.52	0.72	
R9823I9	gneiss	325833	6923822	130/70	210/75	1.7	1.2	prism [c]	0.25	0.23	0.52	0.52	top E
R9824B7	eclogite bo	327304	6923241	140/26	100/30	1.6	1.2	prism [c]?	0.03	0.46	0.50	0.06	
R9826C	gneiss	329191	6914284	146/21	108/29	1.8	1.3	basal <a>	0.09	0.20	0.71		symmetrical
R9828C98	quartzite	313872	6908472	027/55	090/09	4.0	1.8	prism <a>?	0.33	0.35	0.31	0.49	
Y0814I	Ultramylon	361485	6845158	350/24	085/11	8.6	3.1	prism <a>	0.73	0.22	0.05	0.77	top W
Y0815M	quartzite	360353	6849154	023/31	102/05	5.1	2.1	prism <a>	0.58	0.34	0.08	0.63	top W
Y0821D	quartzite	367921	6849700	275/30	267/25	3.0	1.5	prism <a>	0.45	0.28	0.27	0.61	symmetrical
Y0822D	vein	371394	6857253	313/15	271/13	8.3	2.9	prism <a>	0.74	0.23	0.03	0.76	top W
Y0822J	quartzite	366990	6854913	254/22	283/10	4.9	1.9	prism <a>	0.63	0.23	0.14	0.73	top W
Y0824P	quartzite	367499	6858991	306/12	262/09	7.0	2.3	prism <a	0.67	0.27	0.06	0.71	top E
Y0829J	quartzite	348041	6857702	160/25	092/04	3.0	1.6	<a> slip	0.32	0.51	0.17	0.39	top W
Y1518C	vein	352765	6851478	030/41	094/15	3.4	1.7	prism <a>	0.29	0.57	0.13	0.34	top W
Y1524K	vein	375864	6864388	218/50	271/25	5.6	2.1	prism <a>	0.51	0.44	0.05	0.53	top W
Y1526E	anorthosite	369700	6869200	048/52	050/45	1.6	1.1	<a> slip	0.19	0.24	0.57	0.44	top W
Y1530D	quartzite	369620	6860160	205/28	268/13	3.6	1.7	prism <a>	0.49	0.36	0.15	0.58	top W
Y1612D	vein	352725	6868464	172/89	256/08	7.1	2.2	prism [c]	0.50	0.33	0.17	0.60	sinistral
Y1617B5	gneiss	325853	6868800	None		1.3	1.1	prism [c]?	0.13	0.21	0.66		
Y1618E4	anorthosite	314162	6871113	345/63	065/40	1.6	1.2	<a> slip	0.13	0.19	0.68		
Y1706B	vein&gneis	326564	6865755	316/80	225/06	2.4	1.3	prism [c]	0.30	0.22	0.49	0.58	sinistral

Foliation and lineation are given as dip and dip direction; azimuth and plunge.
J[c] and J<a> indicate strength of [c] and <a> axis CPOs
P, G, and R indicate extent to which [c] axis CPO forms a point, girdle, or random distribution.
Pn = P/(P+G). Not calculated for samples with high R values or obscure CPOs.
fsp% includes plagioclase and K-feldspar; "chl", chlorite; "ep", epidote/zoisite; "gar", garnet; "hbl", hornblende; "kspar", K-feldspar;

Appendix 1. Part 2: additional sample attributes.

	quartz	fsp	other		qtz	quartz undulose	subgrain	grain-boundary
	%	%	%	Other minerals	regime	extinction	development	tortuosity
E9730H1	30	60	10	gar, mica, hbl	3	strong	moderate	strong
E9801i1	85	10	5	mica	2	strong	strong	very strong
E9801O1	75	15	10	mica	3	strong	moderate	moderate
E9804H	60	35	5	mica	3	moderate to weak	moderate	weak to moderate
E9805B5	100	0	0			ultramylonite	ultramylonite	ultramylonite
E9805M	50	40	10	mica	3	moderate	moderate to strong	moderate
E9805N	85	10	5	mica	3	moderate	moderate	weak to moderate
E9809C6	20	55	15	mica	3	moderate	moderate	moderate
E9810E	80	15	5	kspar, mica	3	moderate	weak	moderate
E9816B6	30	70	0		3	strong	strong	strong
E9816E	85	10	5	mica	3	moderate	weak to moderate	moderate
E9816F	40	30	30	gar, mica	3	weak	weak	straight to weak
E9818B	80	15	5	mica	3	strong	strong	strong
E9818F2	85	10	5	kspar, mica	2	strong	strong	strong
E9819A	75	25	0	kspar, mica	2 to 3	strong to moderate	strong to moderate	strong
E9820M9	100	0	0		3	strong	strong	strong
E1606L5	100	0	0		3	moderate	moderate	moderate to strong
E1606L6	55	35	10	mica, ep	3	moderate	moderate	straight
E1608G1	30	55	15	mica	3	strong	moderate	strong
E1612C9	20	75	5	mica	3	weak	weak	straight
E1613P	40	50	10	mica, kspar	3	very strong	strong	strong
E1614A7	25	70	5			weak	weak	straight
E1627E	45	50	5	mica	3	strong	moderate	pinned by feldspars
H1604I3	25	70	5	mica, ep, sph	3	moderate	moderate	weak
J2801C	60	40	0	kspar	2 to 3	strong	strong	strong
J2802H1	65	25	10	kspar, mica	2	strong	moderate	very strong
J2802L	65	35	0	kspar	2	strong	moderate	very strong
J2802S2	50	50	0		3	strong	moderate	strong
J2803M	60	30	10	kspar, mica	2	strong	strong	strong
J2804L2	55	10	35	mica, kspar	2 to 3	strong	strong	strong
J2804L31	70	25	5	kspar, mica	2	strong	strong	moderate to strong
J2805S	70	25	5	kspar, mica	2 to 3	strong	strong	strong
J2806A2	70	25	5	kspar, mica	2	strong	strong	strong
J2812A	75	20	0	mica	2	strong	strong	strong

J2813D	85	10	5	kspar, mica	2	strong	strong	strong
J2818J	70	20	10	kspar, mica	2	strong	strong	strong
J2819D	90	0	10	mica	2 to 3	strong	strong	moderate
J3628B	55	45	0		3	moderate	moderate	moderate
J3630D	65	30	5	kspar, mica, sph	2 to 3	moderate	moderate	moderate
J3701E3	75	25	0		2	ultramylonite	ultramylonite	ultramylonite
J3701E4	65	25	10	mica	2	ultramylonite	ultramylonite	ultramylonite
J3705H	75	20	5	kspar, mica	2	strong	moderate	strong
J5814C	20	60	20	mica, chl	3	moderate	pinned	pinned
J5814N2	30	50	20	gar, mica, ky, mica	3	moderate	moderate	moderate
J5815C	20	60	20	gar, mica	3	strong	strong	strong
J5815E4	35	30	30	gar, mica	3	moderate	moderate	weak to moderate
J5815F2	95	0	5	gar, mica	3	moderate	moderate	moderate
J5816L2	85	10	0	kspar, mica	3	weak	moderate	strong
K7708J	95	0	5	mica	3	moderate	moderate	moderate
K7709H6	75	25	0		3	low to moderate	weak	moderate to straight
K7710R1	90	10	0		2	strong	moderate	moderate to strong
K7710R2	80	15	5	mica	2	strong	moderate	moderate to strong
K7710S	60	35	5	mica	2	strong	strong	strong
K7711D	30	55	15	kspar, mica	3	moderate	moderate	moderate to strong
K7711E1	30	30	35	mica	3	strong	strong	strongly strong
K7711E2	100	0	0		2 to 3	strong	strong	strongly strong
K7711E3	80	15	5	mica	3	strong	strong	strongly strong
K7711K	75	20	5	mica, ep	3	moderate	moderate	moderate
K7714A2	35	65	0	kspar	3	moderate	moderate	straight
K7716A	60	25	15	mica, sph	3	moderate	moderate	weak to moderate
K7717A	100	0	0		3	weak	weak	straight
K7717G	55	30	5	mica	3	weak	weak to moderate	straight to weak
K7719A	60	25	15	mica, sph	2	strong	strong	strong
K7721C	75	20	5	hbl, ep	2	strong	moderate	relatively strong
P6803A2	40	30	30	gar, ep, mica, chl	2	very strong	strong	strongly strong
P6807F7	100	0	0		3	weak	weak	straight
P6807F8	30	50	20	hbl, gar, ru	3	strong	strong	moderate
P6807F9	65	10	25	gar, sph	3	weak	weak	straight to weak
P6807G2	25	70	5	mica	3	weak	moderate	straight
P6808A3	60	20	20	mica	3	moderate	moderate	modest
P6809A3	30	65	5	mica, gar	3	moderate	moderate	moderate

P6821D1	35	40	25	gar, mica, chl	3	moderate	weak	relatively strong
P6822B1	35	50	15	gar, mica	3	weak	weak	straight
P6824C1	60	30	10	mica, gar, mica	3	very weak	none	straight
P6824C2	30	60	10	mica	3	weak	weak	straight
P6824C2	100	0	0		3	moderate	moderate	straight to weak
P6826E1	25	75	0		2 to 3	moderate	moderate	moderate to strong
8815G11	10	80	10	gar, hbl, cpx, mica	3	isolated qtz grains	isolated qtz grains	isolated qtz grains
8829A2	30	60	10	kspar	3	weak	weak	straight
8830B9	90	5	5	mica	2 to 3	strong	strong	very strong
R8906B9	80	20	0	mica, opx, gar, ky	3	weak	weak	weak to moderate
R9823F9	35	60	10	kspar, mica	3	weak	moderate to weak	straight to weak
R9823I9	30	65	0	kspar, mica	3	moderate to strong	moderate to strong	straight to weak
R9824B7	30	65	5	gar, hbl, mica, chl	2	strong	strong	strong
R9826C	30	60	10	mica, sph	3	strong	strong	moderate
R9828C98	92	5	0	gar, amph	3	moderate	moderate	weak to moderate
Y0814I	100	0	0		2	strong	strong	strong
Y0815M	90	10	0		3	weak	moderate	straight
Y0821D	55	40	5	mica	2	strong	strong	strong
Y0822D	100	0	0		2 to 3	strong	moderate	strong
Y0822J	65	30	5	mica	2 to 3	moderate	moderate	moderate
Y0824P	85	10	5	mica	2 to 3	strong	strong	very strong
Y0829J	95	0	5	mica	2 to 3	strong	strong	strong
Y1518C	100	0	0		2 to 3	moderate to strong	moderate	moderate
Y1524K	100	0	0		2 to 3	strong	moderate to strong	strong
Y1526E	20	75	5	kspar, mica	3	weak	weak	straight
Y1530D	90	10	0	mica	2 to 3	strong	moderate to strong	strong
Y1612D	100	0	0		3	strong	strong	strong
Y1617B5	25	70	5	mica, sph	3	moderate	moderate	weak to moderate
Y1618E4	5	90	5	kspar, ep, hbl	3	isolated qtz grains	isolated qtz grains	isolated qtz grains
Y1706B	85	15	0		3	strong	strong	strong

fsp% includes plagioclase and K-feldspar; "chl", chlorite; "ep", epidote/zoisite; "gar", garnet; "hbl", hornblende; "kspar", K-feldspar; "ky", kyanite; "opx", orthopyroxene; "ru", rutile; "zo", zoisite.

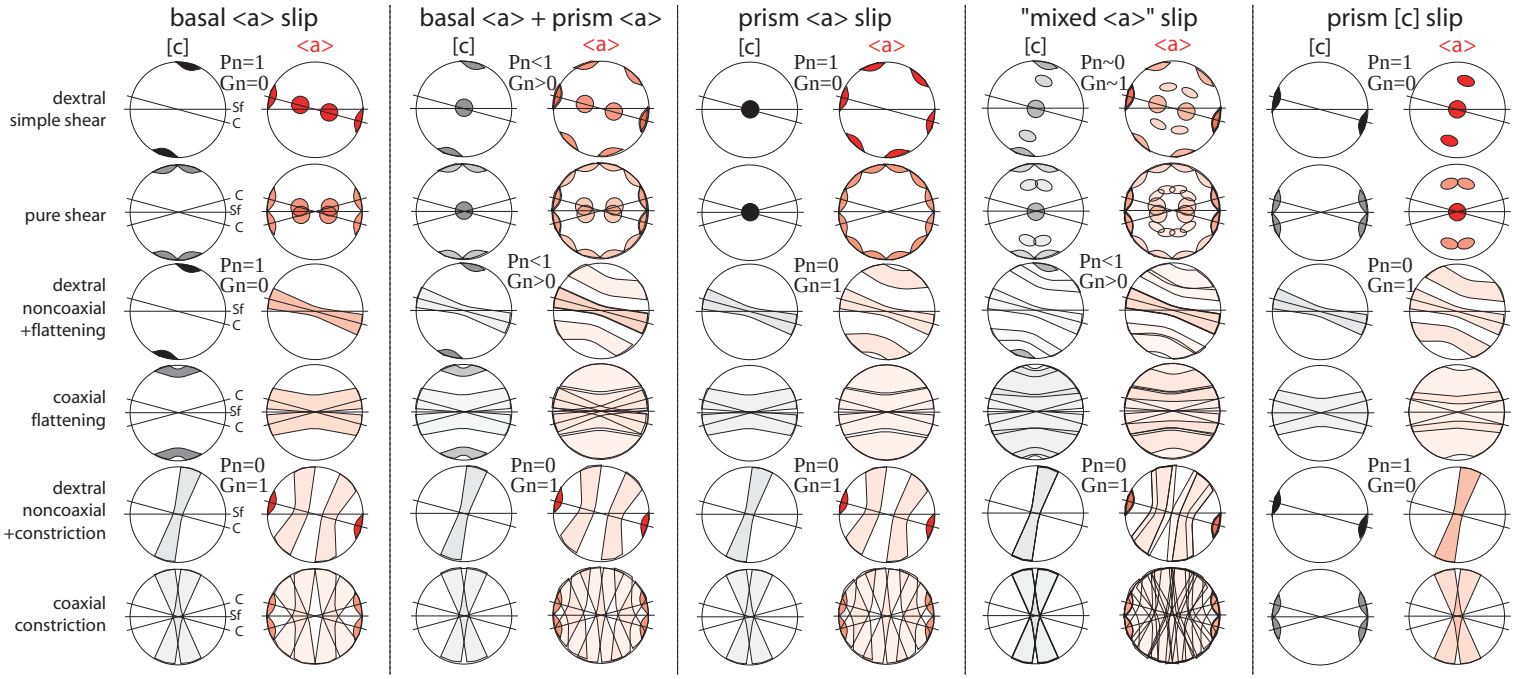

Figure 1. CPOs and Pn and Gn indices expected from various quartz slip systems subjected to different strain geometries. In each stereonet, foliation (Sf) is horizontal, cisaillement (C) planes are inclined, and lineation is at the intersection of the foliation with the primitive (i.e., E-W)

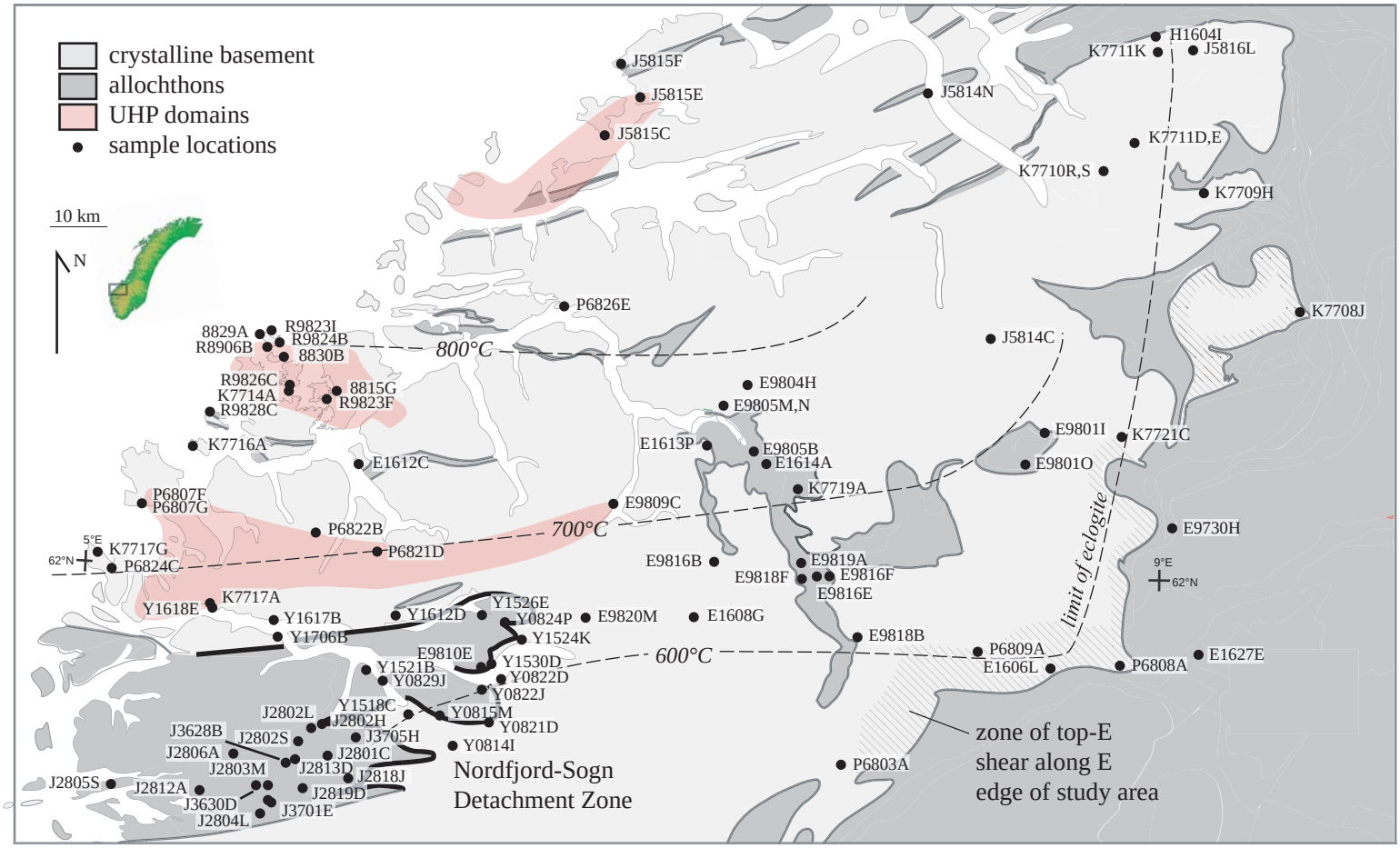

Figure 2. The Western Gneiss Region of Norway consists of a crystalline basement overlain by allochthons emplaced toward the southeast. Major features include the ultrahigh-pressure (UHP) domains, the top-W Nordfjord-Sogn Detachment Zone and the top-E shear zone along the eastern edge of the crystalline basement. Metamorphic temperatures increase toward the northwest [Kylander-Clark et al., 2008].

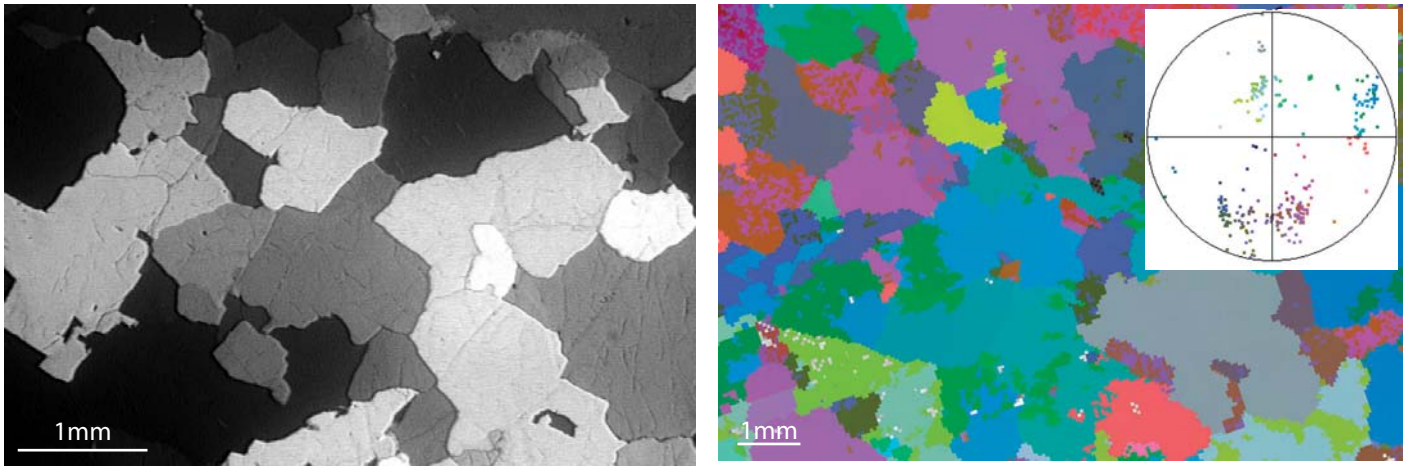

a. Quartz vein P6807F7 showing weak undulatory extinction, weak sub-grain formation, and fairly straight grain boundaries indicative of quartz deformation Regime 3.

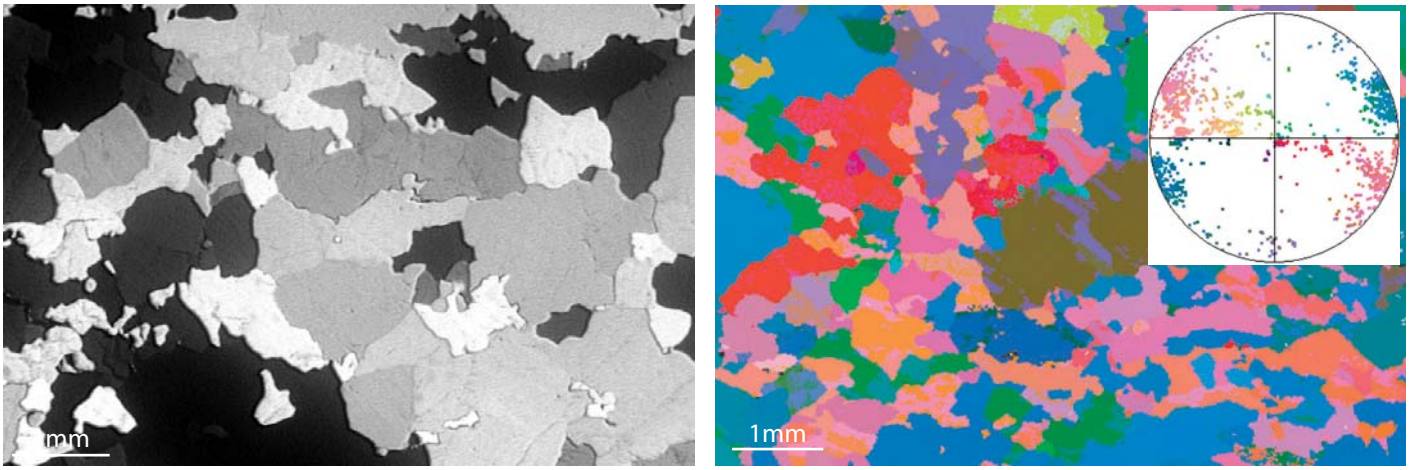

b. Quartz vein in eclogite K7717A2 showing weak undulatory extinction, modest sub-grain formation, and straight grain boundaries indicative of Regime 3.

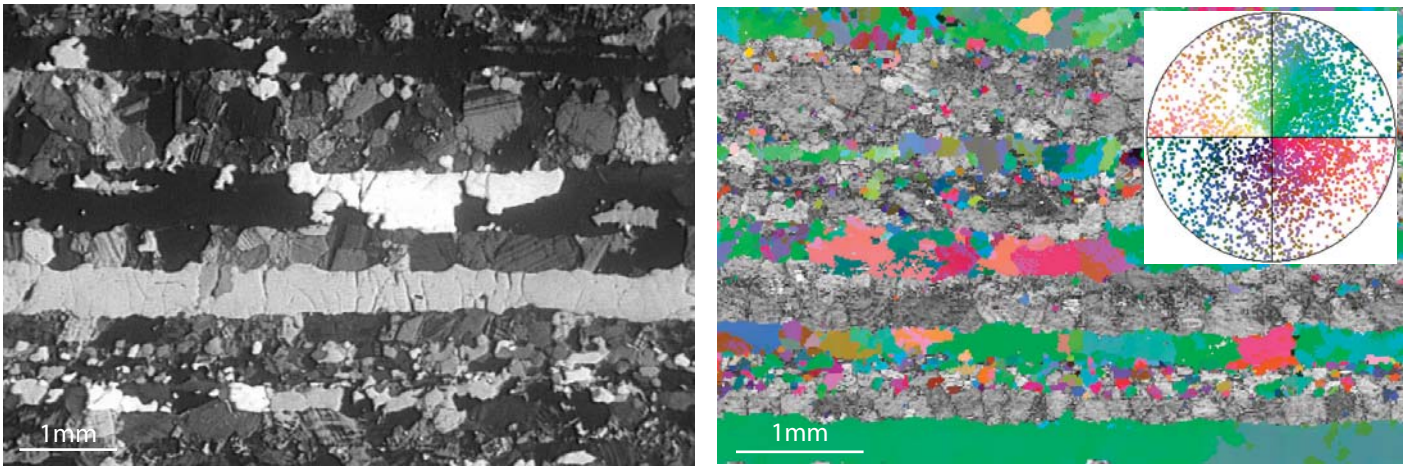

c. Gneiss sample R9823F9 composed of bands of quartz and plagioclase. Regime 3.

Figure 3. Representative microstructures. Optical microstructures (left) are indicative of quartz deformation Regime 2 (a few samples) or 3 (most samples); cross-polarized light. EBSD map colored by crystal orientations shown in [c] axis stereonet (one point per grain).

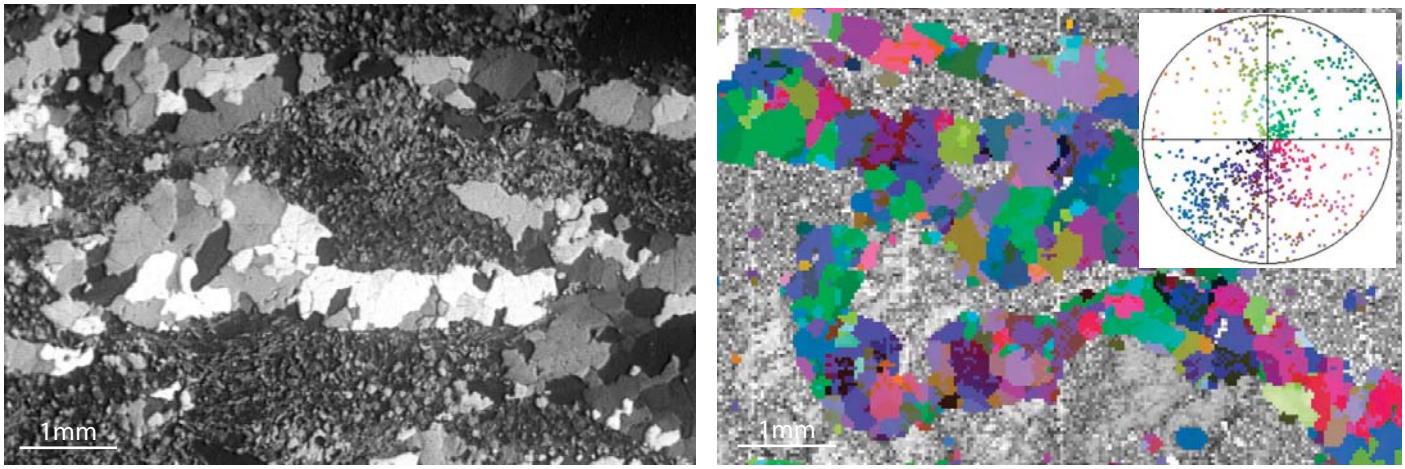

d. Gneiss sample P6821D1 with quartz-rich zones surrounded by fine-grained symplectites. Grain boundaries are dentate. Regime 3.

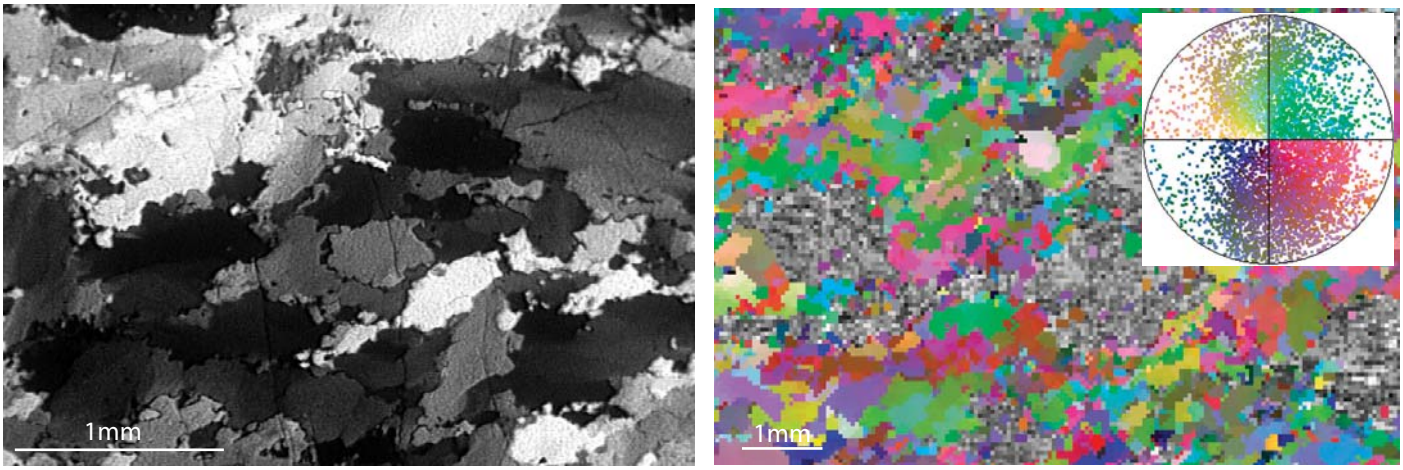

e. Gneiss sample P6803A2 with strong undulatory extinction, strong sub-grain formation, and dentate grain boundaries indicative of sub-grain rotation recrystallization (Regime 2).

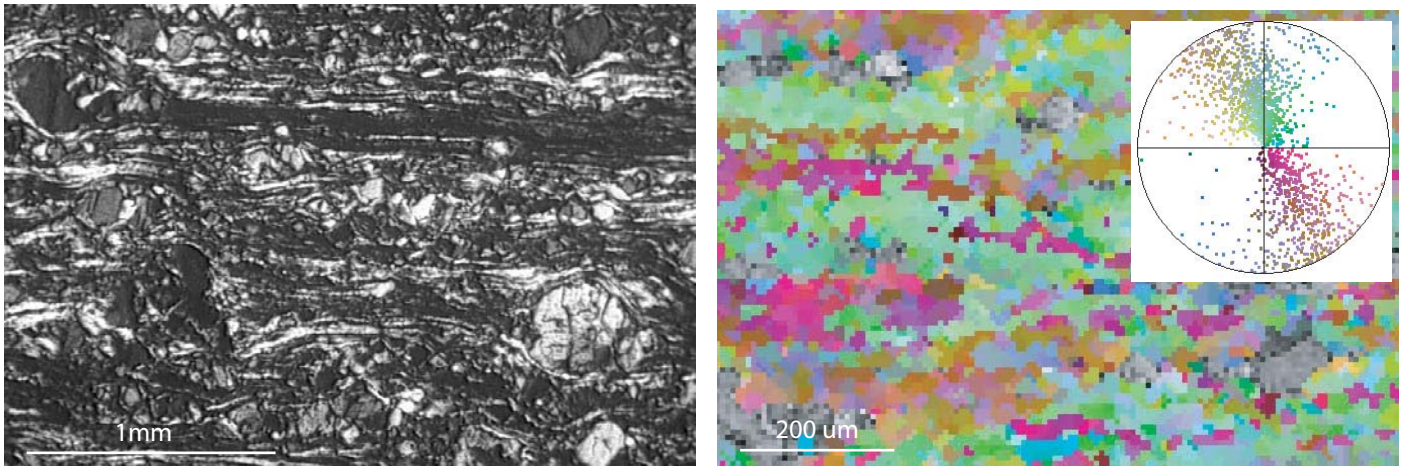

f. Quartz-rich ultramylonite J3701E3 with highly stretched quartz grains and feldspar porphyroclasts. Regime 2.

Figure 3 continued.

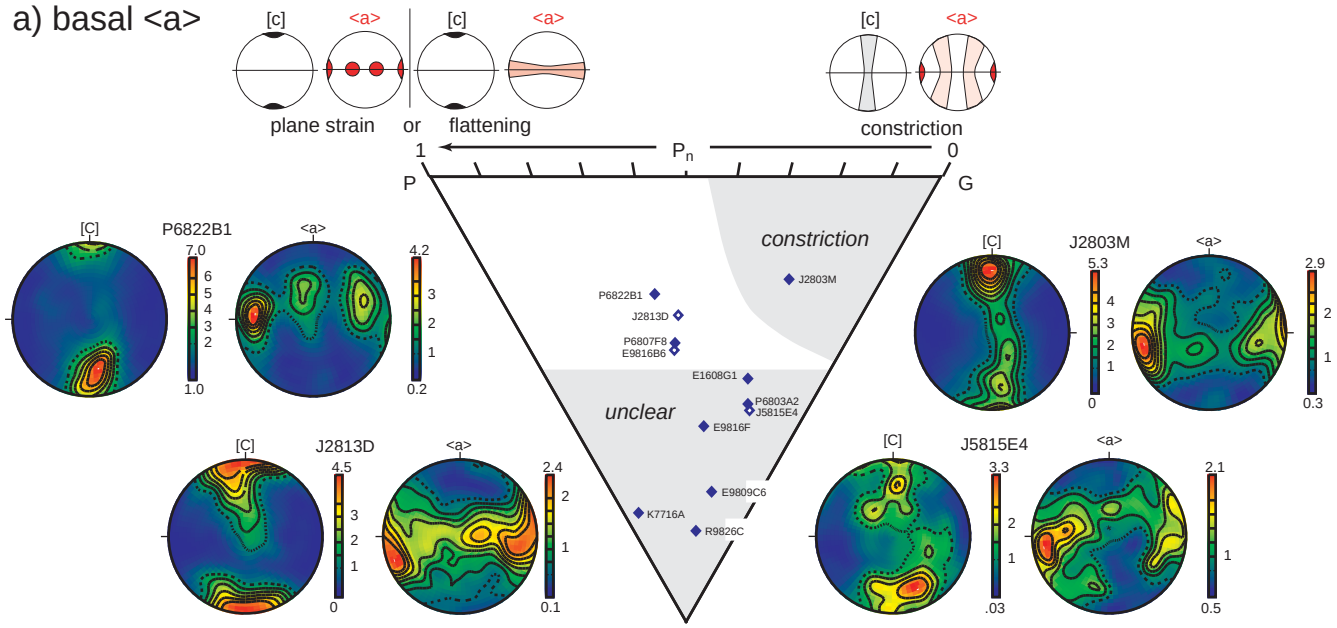

Figure 4. Representative quartz CPOs and calculated P, G, R values. Upper hemisphere projections in which the <a> axes have been collapsed using 622 symmetry. CPOs for other 'J' and 'Y' samples can be found in Johnston et al. [2007b] and Young et al. [in review], respectively. a) CPOs attributable to basal <a> glide have characteristics compatible with plane strain or flattening (4 samples) and constriction (1 sample); another seven samples have more obscure CPOs with high R values. b) CPOs attributable to prism <a> glide have characteristics compatible with a mix of plane strain and constriction, with the former dominant; none are compatible flattening. c) CPOs attributable to "mixed <a>' slip are compatible with constriction and plane strain. d) CPOs attributable to prism [c] slip are compatible with either plane strain (e.g., Y1706B) or constriction (e.g., K7717A).

b) prism <a>

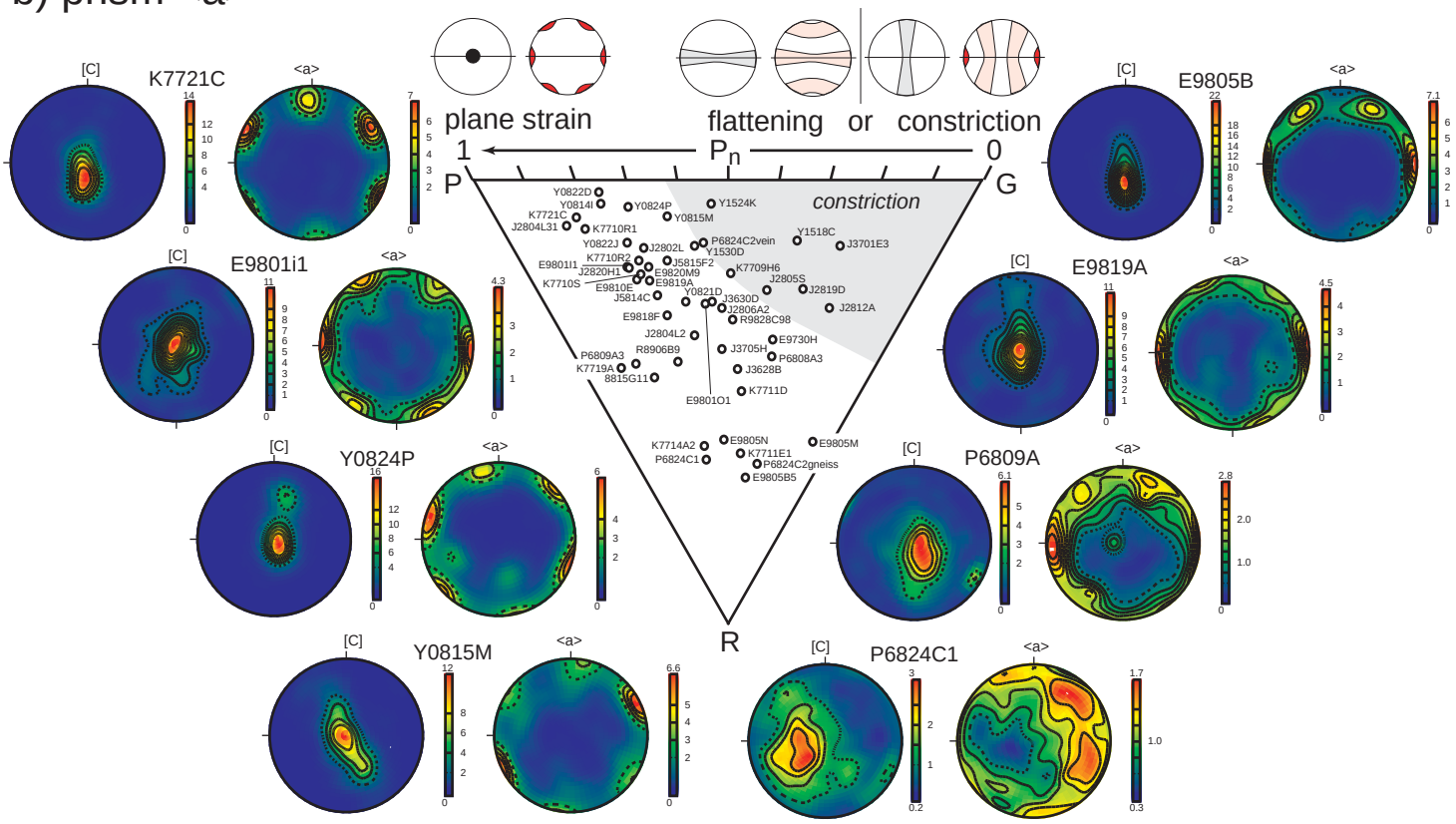
plane strain
flattening or constriction
1
Pn
0
P
G
R
constriction
[C]
<a>
K7721C
E9805B
E9801i1
E9819A
Y0824P
P6809A
Y0815M
P6824C1
Y0822D
Y0814I
Y0824P
Y1524K
K7721C
Y0815M
J2804L31
K7710R1
Y1518C
J3701E3
Y0822J
J2802L
P6824C2vein
Y1530D
E9801i1
K7710R2
J5815F2
K7709H6
J2820H1
E9820M9
K7710S
E9819A
J2805S
E9810E
J2819D
J5814C
Y0821D
J3630D
J2806A2
J2812A
E9818F
R9828C98
J2804L2
E9730H
R8906B9
J3705H
P6809A3
P6808A3
K7719A
J3628B
8815G11
E9801O1
K7711D
K7714A2
E9805N
E9805M
K7711E1
P6824C1
P6824C2gneiss
E9805B5

c) mixed <a> slip

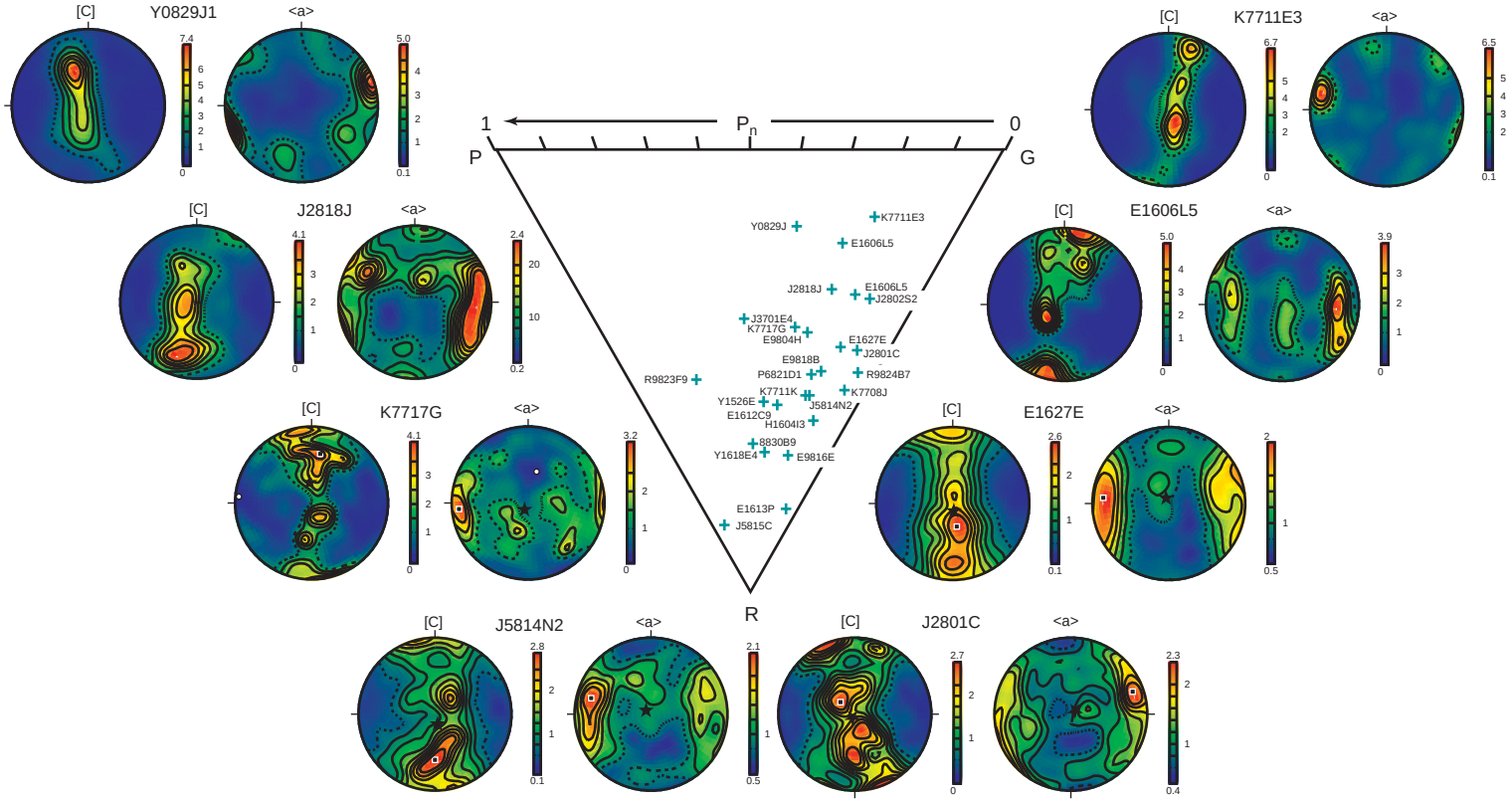

d) prism [c]

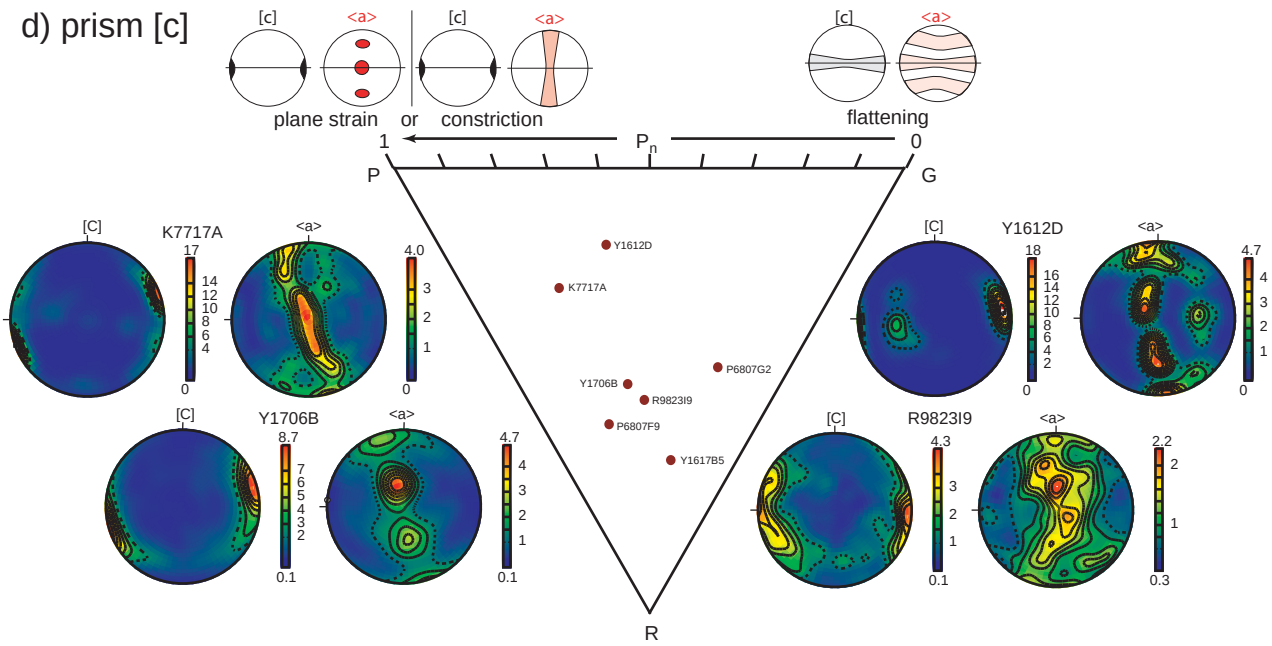
[c]
<a>
[c]
<a>
plane strain
or
constriction
[c]
<a>
flattening
1
Pn
0
P
G
R
[C]
K7717A
<a>
17
14
12
10
8
6
4
0
4.0
3
2
1
0
Y1612D
K7717A
P6807G2
Y1706B
R9823I9
P6807F9
Y1617B5
[C]
Y1612D
<a>
18
16
14
12
10
8
6
4
2
0
4.7
4
3
2
1
0
[C]
Y1706B
<a>
8.7
7
6
5
4
3
2
0.1
4.7
4
3
2
1
0.1
[C]
R9823I9
<a>
4.3
3
2
1
0.1
2.2
2
1
0.3

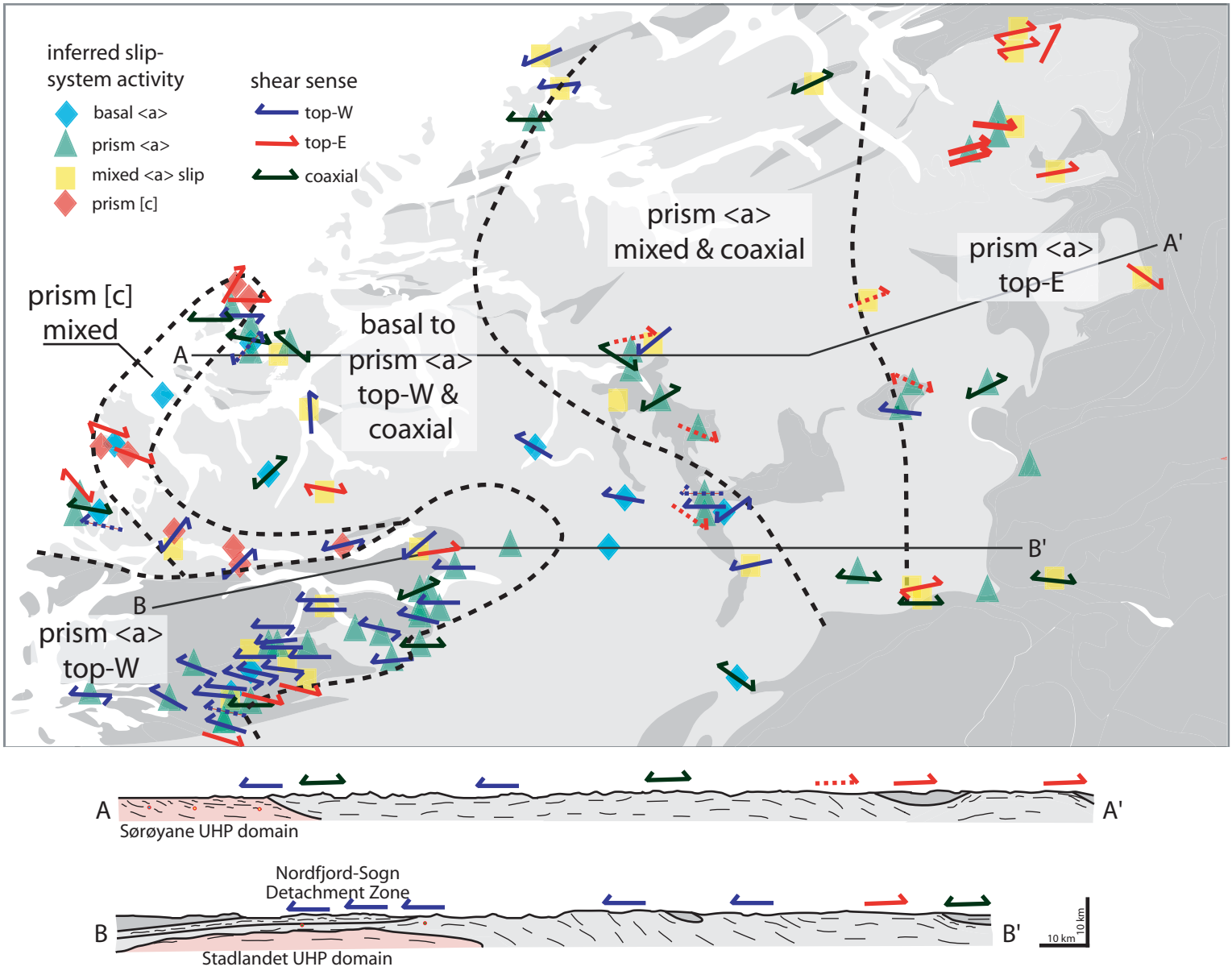

Figure 5. Slip systems and shear sense inferred from CPOs show distinct domains: top-W prism <a> slip along the Nordfjord-Sogn Detachment Zone, mixed prism [c] slip in the west near the southernmost UHP domain, and a transition to top-E shear farther east. Dashed arrows indicate less robust data.

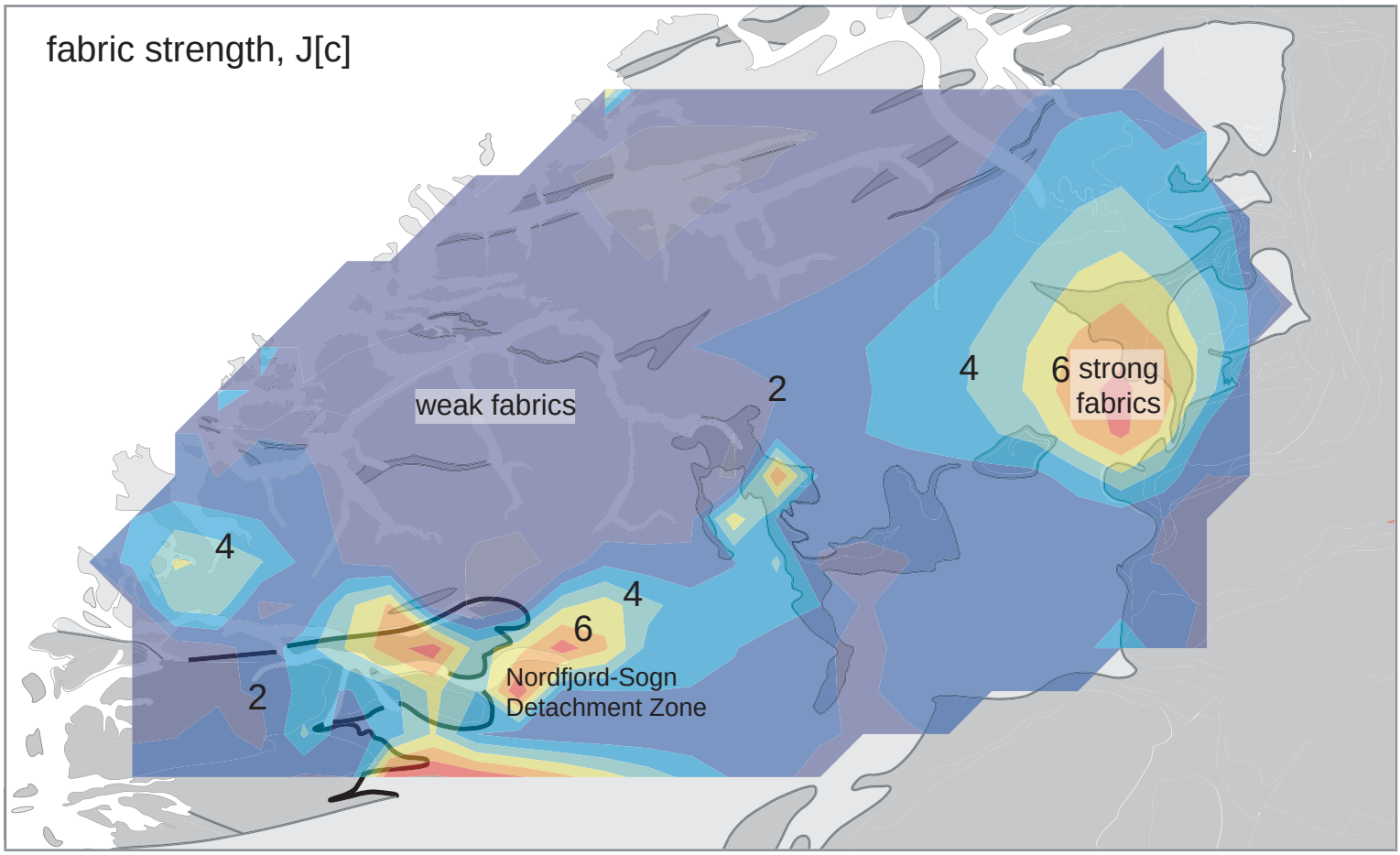

Figure 6. As measured by J[c] value (J<a> is nearly identical and 1-R is similar), CPOs are strongest along the Nordfjord-Sogn Detachment Zone and within the top-E domain in the east. Contoured using the Matlab griddata(cubic) routine.

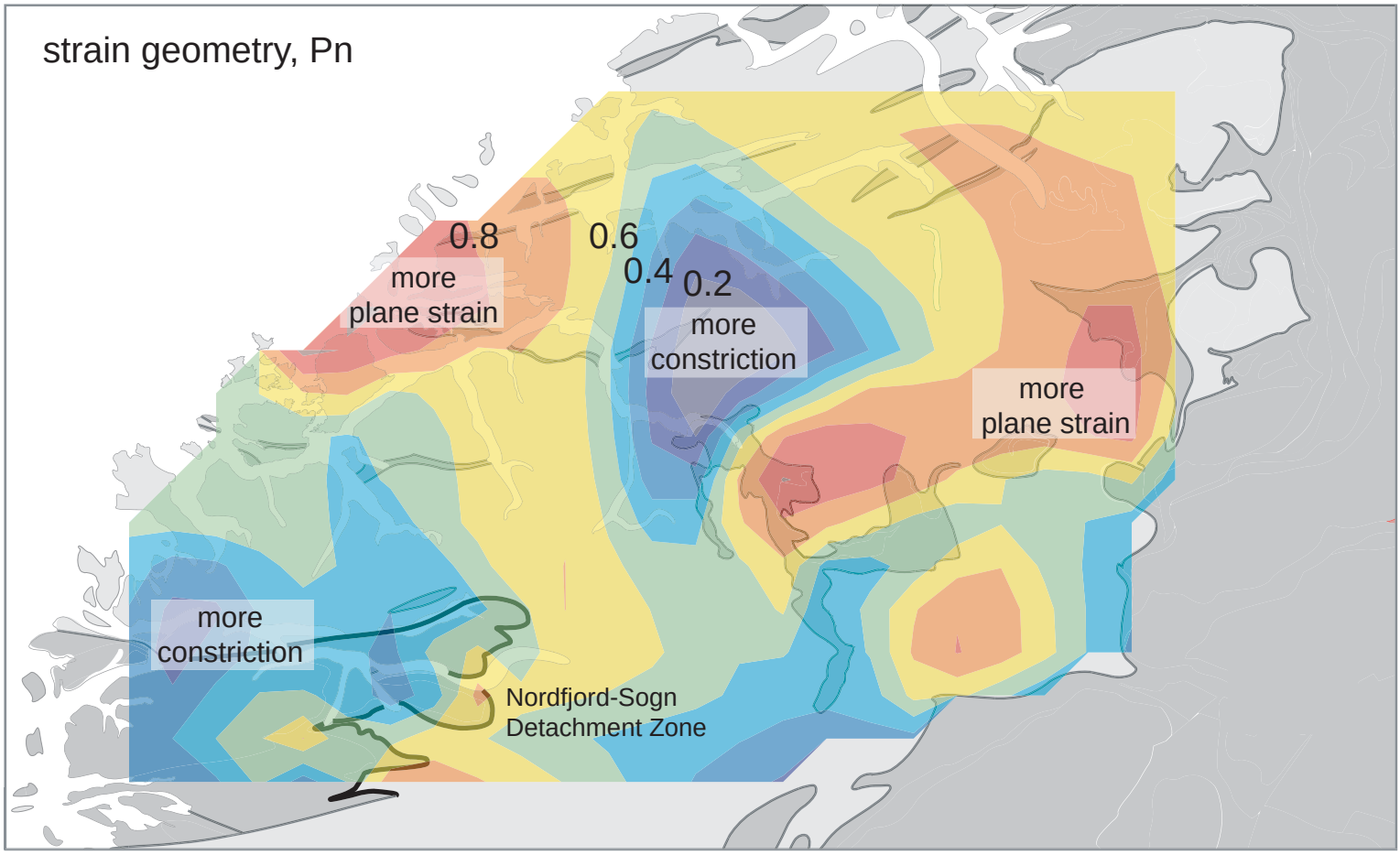

Figure 7. The constrictional component inferred from CPOs using Pn is weakest in the south(east) and strongest in the north(west). Only samples with Pn values listed in the Appendix were used (i.e., samples with large R values or obscure CPOs were excluded). Contoured using the Matlab griddata(cubic) routine.